Depressurization of CO_2 in a pipe: Effect of initial state on non-equilibrium two-phase flow

Alexandra Metallinou Log[b,*], Morten Hammer[a], Han Deng[a], Anders Austegard[a], Armin Hafner[b], Svend Tollak Munkejord[a]

[a]*SINTEF Energy Research, P.O. Box 4761 Torgarden, NO-7465 Trondheim, Norway*
[b]*Norwegian University of Science and Technology, Department of Energy and Process Engineering, NO-7491 Trondheim, Norway*

Abstract

It is key in several industrial applications to accurately describe rapid depressurization of liquid and dense phase states. Examples include refrigeration systems, nuclear reactor cooling and CO_2 capture and storage (CCS). It is expected that large-scale CO_2 pipeline transportation must be deployed as a vital part of reaching net zero emissions by 2050. During rapid depressurization of liquid-like CO_2, boiling will in many cases occur out of equilibrium, at a lower pressure than the local saturation pressure. Capturing the non-equilibrium effects is necessary to predict outflow rates and the resulting pressure and temperature inside the pipe. In the present work, we quantify the non-equilibrium effects by studying a series of CO_2 pipe depressurization experiments from liquid-like states at initial temperatures from $10\,°C$ to $40\,°C$. We compare the experimental results to predictions of the homogeneous equilibrium model (HEM) and a homogeneous relaxation-type non-equilibrium model (HRM*) where the mass-transfer rate from liquid to gas is tuned by a relaxation time. The relaxation time was found to decrease for increasing temperatures, and it was observed to be approximately 60 times longer for the coldest experiment than for the warmest one.

Keywords: carbon dioxide, decompression, flashing flow, non-equilibrium, experiment, boiling flow

---

*Corresponding author.
  Email addresses:* alexandra.m.log@ntnu.no (Alexandra Metallinou Log), alexandra.log@hotmail.com (Alexandra Metallinou Log)

Nomenclature

Latin letters

c	Speed of sound	$\mathrm{m\,s^{-1}}$
$\tilde{C}_p$	Heat capacity	$\mathrm{J\,K^{-1}}$
C_p	Specific heat capacity	$\mathrm{J\,K^{-1}\,kg^{-1}}$
E	Total energy	$\mathrm{J\,m^{-3}}$
e	Specific internal energy	$\mathrm{J\,kg^{-1}}$
$\boldsymbol{F}$	Flux vector	-
$\mathcal{F}$	Friction force	$\mathrm{N\,m^{-3}}$
G	Free energy	J
h	Specific enthalpy	$\mathrm{J\,kg^{-1}}$
J	Nucleation rate	$\mathrm{m^{-3}\,s^{-1}}$
K	Kinetic prefactor	$\mathrm{m^{-3}\,s^{-1}}$
k_B	Boltzmann's constant	$\mathrm{J\,K^{-1}}$
m	Mass	kg
p	Pressure	MPa
Q	Heat	$\mathrm{W\,m^{-3}}$
r	Radius	m
s	Specific entropy	$\mathrm{J\,K^{-1}\,kg^{-1}}$
$\boldsymbol{S}$	Source term vector	-
S	Wave speed estimate for HLLC solver	$\mathrm{m\,s^{-1}}$
T	Temperature	K
t	Time	s
u	Velocity	$\mathrm{m\,s^{-1}}$
$\boldsymbol{U}$	Vector of conserved variables	-
x	Spatial coordinate	m
x_g	Mass fraction of gas	$\mathrm{kg/kg}$

Greek letters

α	Volume fraction	$\mathrm{m^3/m^3}$
Γ	Mass-transfer source	$\mathrm{kg\,m^{-3}\,s^{-1}}$
γ	Grüneisen parameter	$\mathrm{Pa\,m^3\,J^{-1}}$
ρ	Density	$\mathrm{kg\,m^{-3}}$
$\tilde{\rho}$	Number density	$\mathrm{m^{-3}}$
σ	Surface tension	$\mathrm{N\,m^{-1}}$
θ	Relaxation time	s

Subscripts

C	Contact discontinuity
crit	Critical
g	Gas/vapor
i	Index of grid cell/finite volume in finite-volume method
L	Left (of cell boundary)
ℓ	Liquid
R	Right (of cell boundary)
sat	Saturation

Superscripts
n Time step index in finite-volume method
*   Critically-sized embryo of new phase

Abbreviations
BBC   Bernoulli-choking-pressure boundary condition
CCS CO_2 capture and storage
RDF   Running ductile fracture
CNT   Classical nucleation theory
ECCSEL   European Carbon Dioxide Capture and Storage Laboratory Infrastructure
EOS   Equation of state
FVM   Finite-volume method
HEM   Homogeneous equilibrium model
HLLC   Harten-Lax-van Leer Contact
HRM   Homogeneous relaxation model
SHL   Superheat limit

1. Introduction

CO_2 capture and storage (CCS) has been identified as one of the necessary tools to mitigate climate change (IPCC, 2022; IEA, 2021, 2022). IEA (2022) describes a global pathway to reach net zero global emissions by 2050. In this pathway, several gigatonnes of CO_2 must be captured and stored annually. As the CO_2 capture plants and storage sites will generally not be co-located, CO_2 will need to be transported by pipelines, ships or other means. For pipeline transportation, the CO_2 will mostly be in the liquid phase at supercritical pressures (Cosham and Eiber, 2008; Roussanaly *et al.*, 2013). Should the CO_2 be depressurized from this state, it will start boiling. Boiling due to depressurization is often called *flashing*. A depressurization event may occur during planned operations, e.g., when releasing some CO_2 through a pressure relief valve, or as an accident, e.g., due to a pipe fracture. The resulting pressure, temperature, sound speed and mass flow of the CO_2 during the depressurization will be strongly affected by the flashing process. Current engineering tools commonly assume that flashing occurs at equilibrium. However, experimental data indicate that flashing often happens at a lower pressure than expected for an equilibrium process (Pinhasi *et al.*, 2005). These effects need to be accounted for in new engineering tools for the safe and economical design and operation of CO_2-transport pipelines. Similar non-equilibrium considerations are also relevant for, e.g., nuclear reactor cooling systems (Edwards and O'Brien, 1970), refrigeration systems (Banasiak and Hafner, 2013), and other industrial systems operating with compressible fluids that will boil if they are depressurized (Liao and Lucas, 2017).

One of the key safety elements for the design and operation of pipelines with compressible fluids is the prediction of running ductile fracture (RDF). A running ductile fracture is a process where an initial defect in the pipe develops into a fracture which runs along the pipe, sustained by the pressure forces from the escaping fluid, see Aursand *et al.* (2016a). When the depressurization through the fracture causes flashing, the reduction in pressure is abruptly slowed down as vapor is produced and expands. During two-phase flow, a relatively high pressure is maintained and large

forces will be available to sustain an RDF. For large-scale CO_2 pipe rupture tests, the crack-tip pressure has been reported to be over 20% lower than expected based on equilibrium assumptions (Michal *et al.*, 2020). Recent work by Skarsvåg *et al.* (2023) shows that estimates of the crack-tip pressure can be significantly improved by taking into account non-equilibrium flashing. At bends and valves of the pipeline, dry-ice will also form which can cause blockage of the flow and may pose a safety risk. Martynov *et al.* (2018) present experiments and models on the solid formation of CO_2 during depressurization. In the present work, we focus on the first instants of depressurization where the pressure remains above the triple point and dry-ice has not yet formed.

It has been observed in several depressurization experiments with various fluids that flashing occurs out of equilibrium (Pinhasi *et al.*, 2005). Such experiments are also called flashing experiments or blowdown experiments. In such experiments, it is observed that the pressure becomes lower than the local saturation pressure before flashing begins. This is referred to as a "pressure undershoot". Equivalently, the temperature becomes higher than the local boiling-point temperature, and the fluid is denoted as "superheated". Both of these terms, pressure undershoot and superheat, quantify the degree of non-equilibrium reached during the depressurization. In Figure 1, we show an example of a depressurization path where a pressure undershoot is attained and the liquid becomes superheated before flashing begins. Such "delayed" flashing is also observed for CO_2 depressurization experiments and large-scale CO_2 pipe-rupture tests (Botros *et al.*, 2016; Munkejord *et al.*, 2020; Michal *et al.*, 2020).

In order to incorporate delayed flashing in depressurization simulations, non-equilibrium models must be applied. This requires determining appropriate closure relations describing the mass-transfer rates between liquid and gas, which has been shown to be challenging (Pinhasi *et al.*, 2005; Liao and Lucas, 2017). The flashing is governed by an array of complex processes including bubble nucleation, bubble coalescence and break-up and bubble growth. A thorough review on the current challenges in modeling these terms was conducted by Liao and Lucas (2017). In particular the bubble nucleation process, or the onset of flashing, is not fully understood. Though much effort has been made to model the mass-transfer rates, generally some correlation is applied in the end. Furthermore, the correlations tend to be specific to the particular case and fluid for which they were fitted.

Research efforts on the simulation of transient CO_2 depressurization have focused on non-equilibrium models with fairly simple correlations for the mass-transfer rates between the phases that are fitted on a case-to-case basis. Brown *et al.* (2013) tested the homogeneous relaxation model (HRM) and later a two-fluid model (Brown *et al.*, 2014), with simple mass-transfer correlations. The correlations were tuned to individual experiments using "relaxation times". Downar-Zapolski *et al.* (1996) made a correlation for the relaxation time based on water depressurization through nozzles. De Lorenzo *et al.* (2017) slightly modified this correlation to better represents measured pressure undershoots for steam-water depressurization tests. The correlation has also been adapted by Angielczyk *et al.* (2010) for CO_2 based on nozzle-flow measurements of Nakagawa *et al.* (2009). However, the relaxation time correlation requires vapor to be present in the flow, and the data of Nakagawa *et al.* (2009) is limited to three depressurization paths passing close to the critical point
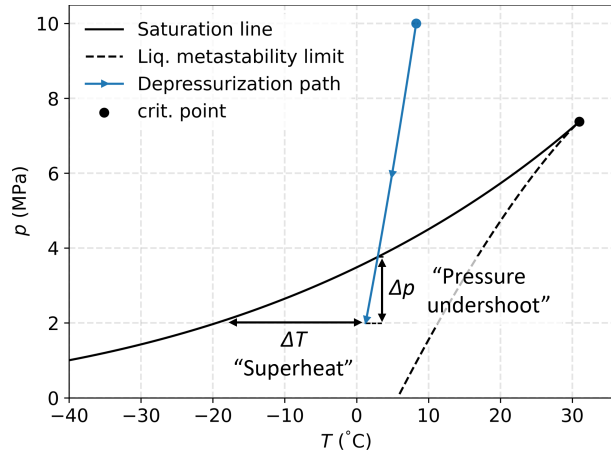
Figure 1: Illustration of a possible depressurization path in the liquid/dense liquid phase before boiling begins in a p-T diagram.

such that the correlation is only valid near the critical point of CO_2.

Later work on the simulation of transient CO_2 depressurization has focused on two-fluid models with a new mass-transfer correlation suggested by Liu *et al.* (2017). This correlation also requires the tuning of a relaxation coefficient to individual cases. Variations of this model have been tested by different authors and validated against data from Test32A of Botros *et al.* (2016), and optimal relaxation coefficients have been found in the range $7\,\text{s}^{-1}$ to $15\,\text{s}^{-1}$ (Liu *et al.*, 2017, 2018; Flechas *et al.*, 2020; Xiao *et al.*, 2020). There is no clear agreement on the choice of relaxation coefficient even for this single depressurization case. Furthermore, as the degree of superheat reached in experiments can vary significantly for different initial conditions (Botros *et al.*, 2016; Munkejord *et al.*, 2020; Quinn *et al.*, 2022), it cannot be expected that the same coefficient value can be applied for different cases. Without a more general correlation or otherwise improved closure relation for the mass-transfer rate between liquid and gas during flashing, the model cannot be applied to make general predictions on the flashing of CO_2 during depressurization.

Hammer *et al.* (2022) applied the theoretical homogeneous superheat limit to predict the outflow of CO_2 through orifices and nozzles, and reached good agreement with experiments. In a study of nozzle flow data for both CO_2 and water, Wilhelmsen and Aasen (2022) found a transition in the mechanism determining the limit of superheat reached (from homogeneous to heterogeneous nucleation) at temperatures a certain distance below the critical point of the fluid. An initial study by Log *et al.* (2022) on some of the experimental data which will be presented in the present paper indicates that this is also the case for CO_2 pipe depressurizations. For depressurization cases with the warmest initial conditions, the maximum degree of superheat reached agreed well with the theoretical homogeneous superheat limit (SHL) estimated by classical nucleation theory. For lower temperatures, the maximum degree of superheat reached was lower than that predicted by the homogeneous SHL. In order to develop models that account for this effect, more depressurization

data are needed for a range of initial temperatures, or rather: initial entropies. Note that this effect is relevant for other fluids in addition to CO_2. Pipe depressurization experiments have been conducted for both water (Barták, 1990) and R-12 (Winters and Merte, 1979) at different initial entropies, but they were all conducted at much colder initial temperatures than the critical point temperature of the fluid, such that the transition in the mechanism determining the limit of superheat was not captured.

As summarized by Munkejord *et al.* (2016, 2020), many rupture and pipe depressurization tests for CO_2 and CO_2-rich mixtures have been conducted and studied (Armstrong and Allason, 2014; Botros *et al.*, 2013; Brown *et al.*, 2014; Clausen *et al.*, 2012; Cosham *et al.*, 2012; Drescher *et al.*, 2014; Jie *et al.*, 2012; Guo *et al.*, 2017; Teng *et al.*, 2016; Gu *et al.*, 2019). More recently, visualization experiments have been conducted to gain further understanding on the non-equilibrium bubble nucleation process during the depressurization of pure CO_2 in vertical (Hansen *et al.*, 2019; Ibrahim *et al.*, 2021) and horizontal ducts (Quinn *et al.*, 2022). For the validation of depressurization simulations, the data of Botros *et al.* (2016, 2017) and Munkejord *et al.* (2020, 2021) are of highest relevance due to the availability of high resolution, high-frequency pressure data. The experimental data of Botros *et al.* (2016) and Munkejord *et al.* (2020) for pure CO_2 cover a sizable range of initial entropies, with three published experiments each. However, the spread in initial entropies for the experiments is quite large. The available data may therefore miss important information on the different boiling processes occurring for different initial entropies, and more data are needed to fully capture how the non-equilibrium phenomena vary in different areas of pressure-temperature space.

In the present work, we present four new pure-CO_2 depressurization experiments conducted at the ECCSEL depressurization facility (ECCSEL, 2021) at a range of initial temperatures complementing our previous experiments (Munkejord *et al.*, 2020). The experiments are intended to provide more knowledge on depressurization events specifically, but they may also help to bring more understanding on flashing flows in general including steady state flows through nozzles and orifices, for which there are large uncertainties related to critical flow during flashing. We study how the non-equilibrium effects change from colder to higher initial temperatures and compare the results to simulations with a simple non-equilibrium model tuned with relaxation times. To provide a reference for the pressure undershoot and degree of superheat observed in the experiments, we also compare the experimental results to simulations using the homogeneous equilibrium model (HEM). The experimental data presented in this paper are openly available and can be downloaded from Zenodo (Log *et al.*, 2023).

The rest of this article is structured as follows: Section 2 provides an overview of the scope of the experimental campaign, the experimental setup and the experimental procedure. Section 3 describes the homogeneous equilibrium and non-equilibrium models. Section 4 presents the numerical solution method of the governing equations. Notably, in Section 4.2 a novel boundary method is suggested which allows for numerical simulations of depressurization cases where the fluid state passes very close to the critical point of the fluid. Section 5 presents experimental and model results, these are analyzed with respect to non-equilibrium effects. Section 6 summarizes the main results and provides concluding remarks.

Table 1: Experimental conditions of the CO_2 depressurization tests.

Test no.	Pressure avg. (MPa)	Temperature avg. (℃)	Ambient temp. (℃)	Figures
4[**]	12.54	21.1	22	9, 10, 15c, 16c, 19e
6[**]	10.40	40.0	6	8, 13a, 14a, 19a
8[**]	12.22	24.6	9	9, 10, 15b, 16b, 19d
19[*]	12.47	10.2	18	9, 10, 15e, 16e, 20b
22[*]	12.48	14.9	14	9, 10, 15d, 16d, 20a
23[*]	12.19	31.5	15	9, 10, 15a, 16a, 19c
24[*]	11.56	35.8	10	8, 13b, 14b, 19b

[*] Present work. [**] Munkejord *et al.* (2020).

2. Scope of test program and experimental setup

In this section, we describe the scope of the test program and provide an overview of the experimental setup. A more detailed description of the experimental setup can be found in Munkejord *et al.* (2020).

2.1. Scope of the test program

In Table 1, we present the experimental conditions of all the depressurization tests studied in the present work. We present four new experiments (Tests 19, 22, 23, 24), and also study three experiments that were introduced by Munkejord *et al.* (2020) (Tests 4, 6 and 8). The complete set of old and new experiments were conducted with initial temperatures approximately ranging from 10 ℃ to 40 ℃ and with an initial pressure of about 12 MPa. An initial study on the data from Tests 19, 4, 8 and 6 showed that there is a transition in the type of bubble nucleation determining the maximum superheat reached for these experiments, where the warmer experiments (Test 4, 8 and 6) agree with the homogeneous superheat limit predicted by classical nucleation theory, and the coldest experiment (Test 19) does not (Log *et al.*, 2022). Details on how the homogeneous superheat limit can be estimated are provided in Appendix A.

An overview of the expected depressurization paths of the tests before boiling begins is plotted with a solid line in a pressure-temperature diagram in Figure 2. We also show in dashed lines the depressurization paths for the metastable liquid states. At temperatures away from the critical point, it is possible to reach further into the metastable liquid area.

2.2. ECCSEL depressurization facility and test procedure

The ECCSEL depressurization facility (ECCSEL, 2021) consists of a gas supply with mass flow controllers, a compression and cooling system for achieving the desired experimental conditions, and a test section with a rupture disk at the open end. The gas supply allows for a secondary gas to be added to the CO_2, but in the present experiments, only pure CO_2 was used. See Munkejord *et al.* (2021) for results for CO_2-rich mixtures. The test section is a tube made of 11 stainless steel pipes providing a total length of 61.67 m. These pipes have an inner diameter of 40.8 mm, an outer diameter of 48.3 mm, and were honed to a mean roughness of $R_a = 0.2\,\mu m - 0.3\,\mu m$.
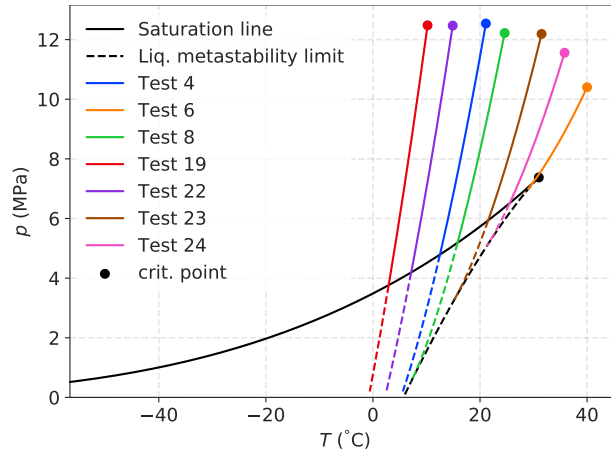
Figure 2: Calculated depressurization paths for the liquid or supercritical state for all the tests presented in Table 1, assuming isentropic flow. The possible metastable parts of the depressurization paths are marked with dashed lines.

The tube is wrapped in heating cables and covered with a 60 mm thick layer of glass wool. The thermal properties of the pipe and insulation layer are provided in Munkejord *et al.* (2020). A P&ID diagram is shown in Figure 3a, providing a schematic overview of the setup. The P&ID is described in detail in Munkejord *et al.* (2020) and we here only provide a brief overview, focusing on the test section and the experimental procedure. The maximum operating pressure of the facility is 20 MPa, and the current design allows experiments with initial temperatures in the range from 5 ℃ to 40 ℃.

A rupture disk with a disk holder is installed at the pipe outlet. The specified burst pressure of the disk is 120 barg ± 5% at 22 ℃. For Tests 4, 6, 8, and 24, X-scored Fike SCRD BT FSR rupture disks were used and for Tests 19, 22, and 23 circular-scored triple-layer Fike HOV BT HL rupture disks were used (see Table 1 for reference on the test numbers). Images of an X-scored rupture disk and a triple-layer disk after a depressurization test is shown in Figure 4. The triple-layered disks were found to open fully more reliably at colder initial temperatures than the X-scored disks, and were therefore applied for later tests to ensure successful experiments. The open membrane area of the rupture disks have a diameter of 63 mm, ensuring that choking will occur at the open end of the pipe. Once the disks are fully open, the depressurizations are expected to be the same for both types of rupture disks.

The experimental procedure is as follows. First, the rupture disk is installed and the system is evacuated. Then the test section is filled with CO_2 and pressurized. When the pressure reaches about 70% of the desired value, the fluid is circulated to achieve a uniform temperature along the test section. The fluid temperature is controlled using heating elements wrapped around the test section. The pressure and temperature are then increased at a controlled rate by alternating filling and circulation of CO_2 until the disk ruptures. Upon disk rupture, the inlet valves at the closed end of the pipe, and outlet valve at the open end of the pipe are automatically

(a) System (RV: relief valve; OV: one-way valve; PV: pneumatic valve)

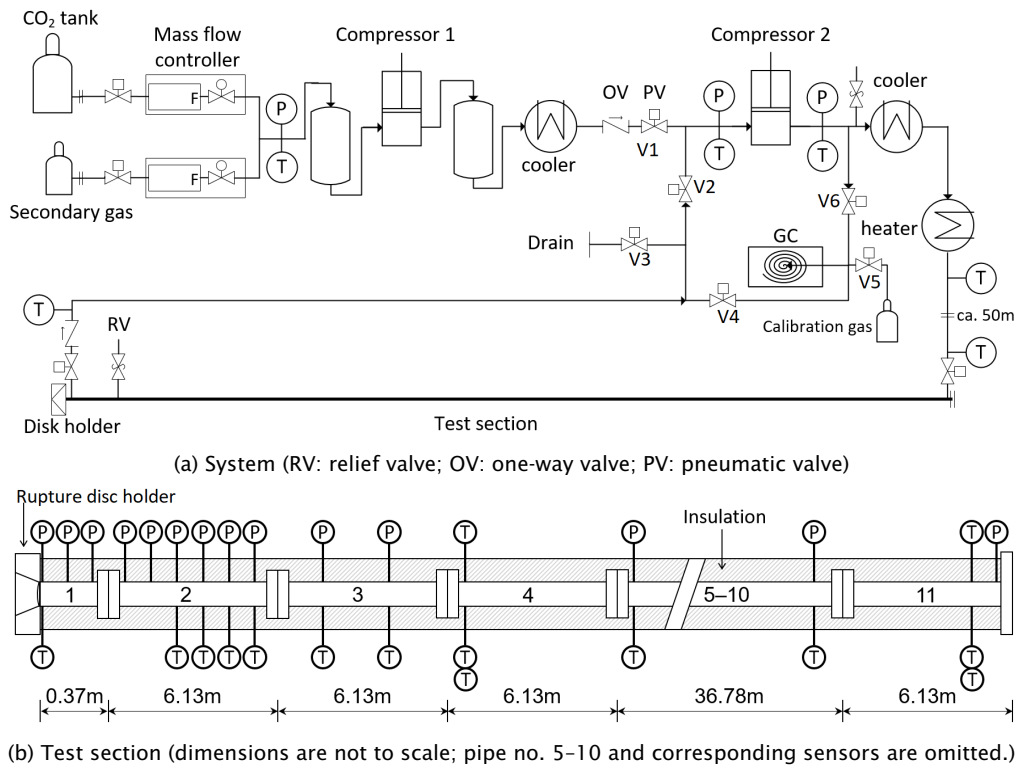(b) Test section (dimensions are not to scale; pipe no. 5–10 and corresponding sensors are omitted.)

Figure 3: Schematic of the ECCSEL depressurization facility.

(a) X-scored rupture disk after test.

(b) Triple-layer rupture disk after test.

Figure 4: Pictures of X-scored and circular-scored triple-layer rupture disks.

Figure 5: CO$_2$ plume released during depressurization test 4.

closed to stop the circulation/filling. The heating cables are also automatically turned off at this point. The released CO$_2$ is vented through an exhaust pipe. An image of the CO$_2$ plume released from Test 4 is shown in Figure 5. The exhaust pipe is designed with a large enough flow area that it will not disturb the flow from the pipe.

2.3. Instrumentation

Along the test section of the facility, 16 fast-response pressure transducers and 23 thermocouples are flush-mounted to the inner surface to capture the pressure and temperature transients during depressurization. The pressure sensors are of the type Kulite CTL-190(M) and the uncertainty of the pressure measurements has been estimated to be around 60 kPa with a confidence interval of 95 % (Munkejord *et al.*, 2020). Most of the pressure sensors are densely distributed close to the open end to capture the depressurization wave, as shown in Figure 3b. Further details regarding the sensors, including a table reporting their locations, can be found in Munkejord *et al.* (2020). In the present work we only report data from three sensors located 8 cm, 28 cm and 49.98 m from the pipe's open end.

The logging frequency of the data from the pressure transducers and thermocouples is 100 kHz and 1 kHz, respectively. The high-frequency data are stored from 0.3 s before disk rupture for a 9 s period. After this period, both pressure and temperature are collected at 50 Hz. The reported initial conditions of the experiments are calculated from the data between 1 ms and 0.5 ms before disk rupture.

For the study of non-equilibrium phase change, the first milliseconds of depressurization are of high importance, as this is the time scale where phase change occurs. For Test 8, the response time of the thermocouples was estimated to be approximately 30 ms (Munkejord *et al.*, 2020). Therefore, only the pressure data are studied in the present work. The complete dataset is made available at Log *et al.* (2023), and will be relevant to validate flow models accounting for the complete depressurization process; capturing the temperature in the pipe, the formation of dry-ice at the closed end of the pipe and dry-out of the liquid. It is beyond the scope of the present work to study these effects.

3. Models

We apply two flow models to analyze the experimental results – a homogeneous equilibrium model (HEM) and a simple homogeneous non-equilibrium model, denoted HRM*. Based on flow visualization experiments (Brown *et al.*, 2013, 2014; Quinn *et al.*, 2022) the flow is likely well-dispersed during the time-scale considered here, so it is reasonable to apply models assuming homogeneously dispersed flow. In the following sections the models are described in more detail.

3.1. Governing equations

3.1.1. The homogeneous equilibrium model

In the homogeneous equilibrium model (HEM) it is assumed that the phases present in the flow travel at the same velocity and are in mechanical, thermal and chemical equilibrium. The governing equations then take the form of the 1D Euler equations for single-phase compressible inviscid flow, with a mass conservation equation, a momentum balance equation and an energy balance equation:

$$\frac{\partial \rho}{\partial t} + \frac{\partial (\rho u)}{\partial x} = 0, \tag{1}$$

$$\frac{\partial (\rho u)}{\partial t} + \frac{\partial (\rho u^2 + p)}{\partial x} = \rho g_x - \mathcal{F}, \tag{2}$$

$$\frac{\partial E}{\partial t} + \frac{\partial ((E + p)u)}{\partial x} = \mathcal{Q}. \tag{3}$$

Here, $\rho = \alpha_g \rho_g + \alpha_\ell \rho_\ell$ is the density of the gas (g) and liquid (ℓ) mixture, u is the common velocity, p the pressure and E the total energy of the mixture.

$$E = \rho \left(e + \frac{1}{2} u^2 \right), \tag{4}$$

where $e = (\alpha_g \rho_g e_g + \alpha_\ell \rho_\ell e_\ell)$ is the specific internal energy of the mixture and α_k denotes the volume fraction of phase $k \in g, \ell$. $\mathcal{F}$ is the pipe wall friction and $\mathcal{Q}$ is the heat transferred from the wall of the pipe to the fluid. g_x is the gravitational acceleration in the axial direction of the pipe. We assume that the pipe is completely horizontal such that $g_x = 0$.

The wall friction is calculated using the Friedel (1979) correlation and the heat transferred from the pipe wall to the fluid is calculated by solving the heat equation in the radial direction in a two-layer domain, as described by Aursand *et al.* (2017). The in-pipe heat-transfer coefficient is estimated based on the Dittus-Boelter correlation, see, e.g., Bejan (1993, Chap. 6) and the outside heat-transfer coefficient is estimated to $4\,\mathrm{W\,m^{-2}\,K^{-1}}$. The main heat transfer effect for the time intervals considered in the present work is directly from the pipe steel to the fluid. To account for the enhanced heat transfer due to boiling, the correlation of Gungor and Winterton (1987) is applied due to its simplicity. For more details on the friction and heat-transfer modeling, see Munkejord *et al.* (2021).

In the numerical solution of the governing equations, the two-phase mixture speed of sound will be needed. The speed of sound is also closely connected to the

depressurization wave speed, $u - c$. The two-phase mixture speed of sound of the HEM can be calculated analytically to be

$$
c_{\text{HEM}} = \left[\rho \left(\frac{\alpha_g}{\rho_g c_g^2} + \frac{\alpha_\ell}{\rho_\ell c_\ell^2} + T\tilde{C}_{p,g} \left(\frac{\frac{1}{\rho_\ell} - \frac{1}{\rho_g}}{h_g - h_\ell} + \frac{\gamma_g}{\rho_g c_g^2} \right)^2 \right. \right.
$$
$$
\left. \left. + T\tilde{C}_{p,\ell} \left(\frac{\frac{1}{\rho_\ell} - \frac{1}{\rho_g}}{h_g - h_\ell} - \frac{\gamma_\ell}{\rho_\ell c_\ell^2} \right)^2 \right) \right]^{-1/2}, \quad (5)
$$

where $c_k = \left(\frac{\partial p_k}{\partial \rho_k} \right)_{s_k}$ is the speed of sound, γ_k the Grüneisen parameter,

$$
\gamma_k = \frac{1}{\rho_k} \left(\frac{\partial p_k}{\partial e_k} \right)_{\rho_k}, \quad (6)
$$

$\tilde{C}_{p,k}$ the extensive heat capacity

$$
\tilde{C}_{p,k} = \alpha_k \rho_k C_{p,k}, \quad (7)
$$

and $C_{p,k}$ is the specific heat capacity of phase k (Flåtten and Lund, 2011, Sec. 6) for a general equation of state.

3.1.2. The simplified homogeneous relaxation model

In the HEM, full equilibrium is assumed between the phases. However, during rapid depressurization, the finite mass-transfer rate between the phases is not always fast enough for equilibrium to be maintained. This can be accounted for by allowing for some non-equilibrium between the phases. We choose here to apply a simplified homogeneous relaxation model, which we denote HRM*, where chemical non-equilibrium is allowed between the phases. Otherwise, we apply the same assumptions as in the HEM. For the standard HRM, it is assumed that $T_g = T_{\text{sat}}(p) \neq T_\ell$. For the HRM*, we apply the simpler assumption that $T_g = T_\ell$. With this simpler assumption, the HRM* belongs in a hierarchy of relaxation models studied by, e.g., (Flåtten and Lund, 2011; Lund, 2012; Linga and Flåtten, 2019), where the HRM* is referred to as the pT-relaxed model. The model has been applied by, e.g., Lund and Aursand (2012); Le Martelot *et al.* (2014); Saurel *et al.* (2016); Pelanti (2022) to simulate boiling flows out of equilibrium.

The HRM* consists of four equations describing the mass balance of gas, mass balance of liquid, the conservation of momentum for the two-phase mixture and the conservation of total energy for the mixture:

$$
\frac{\partial(\alpha_g \rho_g)}{\partial t} + \frac{\partial(\alpha_g \rho_g u)}{\partial x} = \Gamma, \quad (8)
$$

$$
\frac{\partial(\alpha_\ell \rho_\ell)}{\partial t} + \frac{\partial(\alpha_\ell \rho_\ell u)}{\partial x} = -\Gamma, \quad (9)
$$

$$
\frac{\partial(\rho u)}{\partial t} + \frac{\partial(\rho u^2 + p)}{\partial x} = \rho g_x - \mathcal{F}, \quad (10)
$$

$$
\frac{\partial E}{\partial t} + \frac{\partial((E + p)u)}{\partial x} = \mathcal{Q}, \quad (11)
$$

12

where Γ is the mass-transfer rate between the phases. For an infinitely fast mass-transfer rate, the HRM* relaxes to the HEM. The frozen two-phase mixture speed of sound of the HRM* can be calculated analytically as

$$c_{\mathrm{HRM}^*} = \left[\rho \left(\frac{\alpha_g}{\rho_g c_g^2} + \frac{\alpha_l}{\rho_l c_l^2} + T \frac{\tilde{C}_{p,g} \tilde{C}_{p,l}}{\tilde{C}_{p,g} + \tilde{C}_{p,l}} \left(\frac{\gamma_g}{\rho_g c_g^2} - \frac{\gamma_l}{\rho_l c_l^2} \right)^2 \right) \right]^{-1/2}, \qquad (12)$$

Lund (2012, Eq. 6.6) for a general equation of state. Here, frozen refers to the mass fraction of gas being assumed constant. As the HRM* relaxes towards the HEM, the speed of sound of the model will always be greater than or equal to the speed of sound in the HEM (Flåtten and Lund, 2011; Lund, 2012). This is referred to as the subcharacteristic condition.

The mass-transfer source, Γ, is modeled as

$$\Gamma = \rho \frac{x_{g,\mathrm{sat}} - x_g}{\theta}, \qquad (13)$$

where $x_g = \dfrac{\alpha_g \rho_g}{\rho}$ is the mass fraction of gas, $x_{g,\mathrm{sat}}$ is the saturated mass fraction of gas and θ is a relaxation time > 0. In this work, θ is modeled as a constant value, fitted for each experiment.

This formulation of the mass-transfer source is general for any relaxation process and has been applied by several researchers to model systems relaxing towards an equilibrium state, including Einstein (1920) as noted by Bilicki and Kestin (1990). The formulation assumes a linear approximation of the relaxation evolution. As shown by Bilicki and Kestin (1990), the mass-transfer source (13) provides a local and instantaneous exponential tendency towards equilibrium from some initial mass fraction $x_{g,0}$,

$$x = x_{g,\mathrm{sat}} - (x_{g,\mathrm{sat}} - x_{g,0}) \exp{(t/\theta)}. \qquad (14)$$

3.2. Thermophysical property models

The thermodynamic properties of the two-phase mixture are obtained with our in-house framework (Wilhelmsen *et al.*, 2017; Hammer *et al.*, 2020) using the GERG-2008 (Kunz and Wagner, 2012) equation of state (EOS). A version of this framework which includes the GERG-2008 EOS has been made openly available (Hammer *et al.*, 2023). The EOS is used to calculate the densities and energies of the existing phases in both the stable and metastable region. The stability limits of the phases, the spinodals, are also calculated using the GERG-2008 EOS and are defined by

$$\left(\frac{\partial p_k}{\partial \rho_k} \right)_{T_k} = 0, \; k \in g, \ell. \qquad (15)$$

The unstable region is never reached for any of the phases.

Due to numerical issues near the critical point for the HEM simulations of Test 6 with the GERG-2008 EOS, we instead employed the Span and Wagner (1996) EOS. We note that the difference between the GERG-2008 EOS and the Span-Wagner EOS on the predicted pressures was in the order of 0.01 MPa and can be considered negligible for our analysis.

13

4. Numerical methods

4.1. Numerical discretization

We now consider the numerical solution of the models, focusing on the HRM*. The governing equations, (8)–(11), can be written in the vectorial form

$$\frac{\partial \boldsymbol{U}}{\partial t} + \frac{\partial \boldsymbol{F}}{\partial x} = \boldsymbol{S}, \tag{16}$$

where

$$\boldsymbol{U} = \begin{pmatrix} \alpha_g \rho_g \\ \alpha_\ell \rho_\ell \\ \rho u \\ E \end{pmatrix}, \ \boldsymbol{F}(\boldsymbol{U}) = \begin{pmatrix} \alpha_g \rho_g u \\ \alpha_\ell \rho_\ell u \\ \rho u^2 + p \\ (E + p)u \end{pmatrix}, \ \boldsymbol{S} = \begin{pmatrix} \Gamma \\ -\Gamma \\ \rho g_x - \mathcal{F} \\ \mathcal{Q} \end{pmatrix}.$$

The mass-transfer source term, Γ, can be stiff, which can cause instabilities in numerical solvers unless special consideration is taken in the solution of the system. The system (16) is therefore solved using a classical first-order fractional step method known as Godunov splitting (LeVeque, 2002, Ch. 17), which is often applied for stiff source terms. In Godunov splitting, two steps are applied to reach the solution. First the homogeneous part of the system is solved without the source term,

$$\frac{\partial \boldsymbol{U}}{\partial t} + \frac{\partial \boldsymbol{F}}{\partial x} = \boldsymbol{0}. \tag{17}$$

The solution of the first step is then applied in the second "relaxation" step, where the following ODE is solved

$$\frac{\mathrm{d}\boldsymbol{U}}{\mathrm{d}t} = \boldsymbol{S}(\boldsymbol{U}). \tag{18}$$

The homogeneous part of the system is solved using the Harten-Lax-van Leer Contact (HLLC) finite-volume method (FVM) (Toro *et al.*, 1994) in space and explicit Euler in time. For the FVM, the 1D computational domain is split into equidistant grid cells of length $\Delta x = \frac{L}{N}$, where L is the length of the pipe and N is the number of grid cells. At each time-step n, the variables in grid cell i are updated by

$$\boldsymbol{U}_i^{n+1} = \boldsymbol{U}_i^n - \frac{\Delta t}{\Delta x}(\boldsymbol{\mathcal{F}}_{i+1/2}^n - \boldsymbol{\mathcal{F}}_{i-1/2}^n) \tag{19}$$

where $\boldsymbol{\mathcal{F}}_{i\pm 1/2}$ are fluxes through the left and right edges of the grid cells, estimated using HLLC.

The HLLC FVM takes the following form for the HRM*:

$$\boldsymbol{\mathcal{F}}_{i+1/2} = \begin{cases} \boldsymbol{F}_L, & \text{if } 0 < S_L, \\ \boldsymbol{F}_L^{\text{HLLC}}, & \text{if } S_L \leq 0 < S_C, \\ \boldsymbol{F}_R^{\text{HLLC}}, & \text{if } S_C \leq 0 < S_R, \\ \boldsymbol{F}_R, & \text{if } 0 \geq S_R, \end{cases} \tag{20}$$

where

$$\boldsymbol{F}_K^{\text{HLLC}} = \boldsymbol{F}_K + S_K(\boldsymbol{U}_K^{\text{HLLC}} - \boldsymbol{U}_K), \tag{21}$$

14

$$U_K^{\text{HLLC}} = \left(\frac{S_K - u_K}{S_K - S_C} \right) \begin{pmatrix} (\alpha_g \rho_g)_K \\ (\alpha_\ell \rho_\ell)_K \\ \rho_K S_C \\ E_K + (S_C - u_K)\left(\rho_K S_C + \dfrac{p_K}{(S_K - u_K)} \right) \end{pmatrix}, \; K = R, L, \qquad (22)$$

and

$$S_C = \frac{p_R - p_L + \rho_L u_L (S_L - u_L) - \rho_R u_R (S_R - u_R)}{\rho_L (S_L - u_L) - \rho_R (S_R - u_R)}. \qquad (23)$$

The subscripts L and R refer to the grid cells with index i and $i + 1$ respectively, i.e. they refer to the grid cell to the left or to the right of the cell face at $i + 1/2$. The left and right wave speeds S_L and S_R must be estimated. In the present work, the simple estimate of Davis (1988) is applied,

$$S_L = \min\left(u_L - c_L, u_R - c_R \right), \; S_R = \max\left(u_L + c_L, u_R + c_R \right), \qquad (24)$$

where c_L and c_R denote the two-phase mixture speed of sound to the left and to the right of the cell boundary. Finally, the remaining ODE (18) is solved with backward Euler using Newton-Raphson iterations.

For the HEM, the HLLC scheme is applied as proposed by Toro *et al.* (1994) for the Euler equations. The solution is integrated in time using the explicit Euler method. Aside from the special consideration made to discretize the mass-transfer source term for HRM*, the numerical solution method for the HRM* and HEM are equivalent. For both models, the numerical solution method is first order accurate in time and space.

4.2. Boundary conditions

At the closed end of the pipe, the boundary condition $u = 0$ is set. This is enabled by a mirror ghost cell.

At the open end, a Bernoulli-choking-pressure boundary condition (BBC) is applied using a ghost cell. We here take the open end to be at the left end of the computational domain. The BBC is described by Munkejord and Hammer (2015) for HEM where it was found to provide overlapping results with a characteristics-based pressure BC at reduced computational cost (see their Fig. 8). For HEM, the BBC is based on the assumption that the flow will be in equilibrium.

For the HRM* we instead assume that the minimum amount of flashing occurs, i.e., either frozen flow with no phase change or the minimum amount of flashing to keep the fluid state within the spinodals of the phases. This provides the minimum possible choking pressure in the ghost cell. With this assumption, the pressure in the ghost cell will always be lower or equal to the pressure in the computational domain and thus it cannot restrain the obtained non-equilibrium in the computational domain. This is an advantage because any relaxation time can be tested in the mass transfer model for HRM* with the certainty that the BC will not restrain the non-equilibrium effects. We denote this BC as the "minimum BBC".

The minimum BBC is set in the following way: we extrapolate the specific entropy, mass fraction and flow speed from the first cell in the computational domain to the

ghost cell:

$$x_{g,0} = x_{g,1} = x_g, \tag{25}$$

$$s_0 = s_1 = s, \tag{26}$$

$$u_0 = u_1 \tag{27}$$

where the subscript 1 denotes the index of the first cell in the computational domain and the subscript 0 denotes the index of the ghost cell, to the left of cell 1. The maximum of the Bernoulli-choking pressure and the atmospheric pressure is then set in the ghost cell:

$$p_0 = \max(p_{\text{BBC}}, p_{\text{atm}}). \tag{28}$$

Munkejord and Hammer (2015) and Log (2020) (see Fig. 4.42, Naive BC) showed that setting the atmospheric pressure in the ghost cell directly can cause the numerical solver to overestimate the fluid's acceleration at the open end of the pipe, leading to too low temperature estimates and a flow with a Mach number u/c higher than 1. For the steady state assumption, the flow cannot accelerate further than to its choking pressure, so it is reasonable to set the choking pressure in the ghost cell, provided that the flow chokes above the atmospheric pressure.

The Bernoulli choking pressure can be estimated using a steady-state flow assumption and applying the Bernoulli equation for compressible flow,

$$\frac{1}{2}u(p, s_1, x_{g,1})^2 + h(p, s_1, x_{g,1}) = \frac{1}{2}u_1^2 + h_1 \tag{29}$$

which defines u as a function of pressure, where h denotes the specific enthalpy of the mixture. The Bernoulli choking pressure is found by solving

$$u(p_{\text{BBC}}, s_1, x_{g,1}) - c(p_{\text{BBC}}, s_1, x_{g,1}) = 0 \tag{30}$$

for p_{BBC} using the bisection method, where $u(p_{\text{BBC}}, s_1, x_{g,1})$ is given by Equation (29).

In some cases, choking does not occur for pressures above the spinodal, where the liquid phase becomes thermodynamically unstable. This is particularly an issue for depressurization simulations where the depressurization path passes close to the critical point. In such a case, no solution exists for p_{BBC}. No stable state exists for the frozen flow at atmospheric pressure either, so atmospheric pressure cannot be set directly.

We avoid the above problem as follows: At the liquid spinodal, liquid would flash instantaneously. We then assume that the minimum amount of flashing will occur if the liquid spinodal is reached. We further assume that the entropy will stay constant:

$$x_{g,0} = x_{g,\min}(p, s_1). \tag{31}$$

An illustration of the problem and our solution is shown in Figure 6. With this method, we will "walk" along the liquid spinodal when searching for the choking pressure, providing the lowest possible Bernoulli choking pressure for nearly frozen flow. We emphasize that this "walk" along the spinodal does not occur *at* the
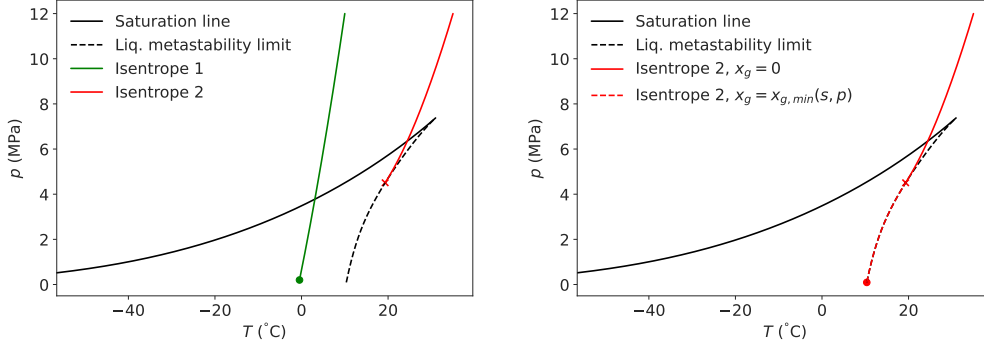
(a) Isentrope 1 does not cross the liquid spinodal. Isentrope 2 crosses the liquid spinodal and needs special consideration when searching for the choking pressure.

(b) For Isentrope 2 the minimum BBC continues the search for a choking point along the liquid spinodal.

Figure 6: Illustration of a case where special consideration must be taken to search for the choking pressure in the BBC approach (Isentrope 2). For the minimum BBC, we add a minimum amount of gas, $x_{g,\text{min}}(s, p)$, "walking along" the metastability limit to find the choking point.

outflow boundary where the HLLC method estimates the resulting flow, it is simply a means to search for the minimum Bernoulli-choking pressure in the ghost cell while avoiding the unstable region of the phases.

We finally note that an increase in the mass fraction of gas would also involve a small increase in the entropy of the fluid. For simplicity, we ignore this entropy increase. The effect of a too low entropy in the outflow ghost cell is negligible inside the computational domain, as analysis of the flow equations shows that entropy is carried with the flow out of the pipe (and not into it).

5. Results and discussion

In this section, we will present the results of the new full-bore depressurization tests and compare the results to previous full-bore depressurization tests (Munkejord *et al.*, 2020). We will then analyze the effect of the initial temperature of the depressurization experiments by comparing the experimental data to computations employing the HRM* and HEM models.

5.1. Experimental results

We first compare the experimental results, focusing on how the different initial temperatures affects the depressurization and non-equilibrium phase change. As explained in Section 2.3, we will only focus on the pressure measurements and on the millisecond time-frame, as this is most relevant to study the flashing out of equilibrium. The initial conditions of the depressurization experiments are listed in Table 1.
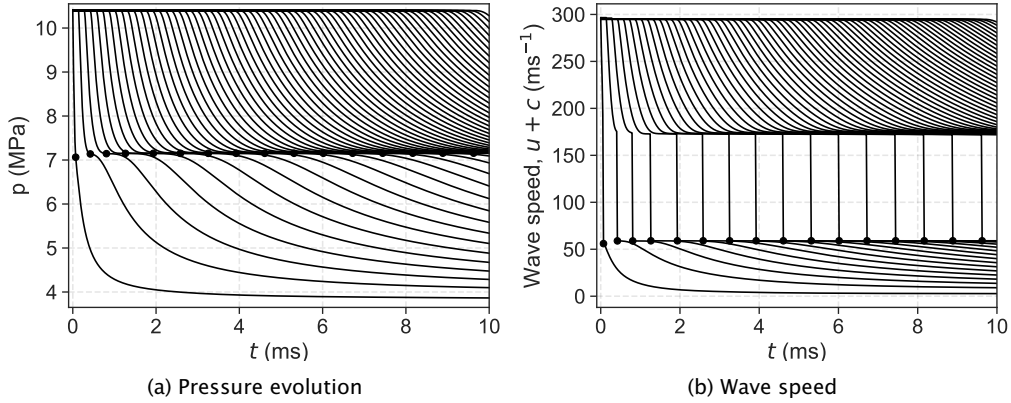
(a) Pressure evolution

(b) Wave speed

Figure 7: Pressure and wave speed over time for a HEM simulation of Test 6 for positions from 0.03 m (leftmost) to 3.20 m (rightmost) from the open end. A marker illustrates where flashing begins in each grid cell.

We observe a clear difference between the pressure measurements near the pipe outlet for the two warmest experiments compared to the colder experiments, due to how choking occurs. Therefore, the results of the warmest experiments and the colder experiments are shown and discussed separately.

The pressure recordings over time at the different positions in the pipe provide information on the local wave speed $u + c$ of the depressurization wave traveling into the pipe. We generally observe a strong decrease in the wave speed once two-phase flow begins, due to a decrease in the speed of sound. In Figure 7, we show an example of how the pressure and wave speed are related using a HEM simulation with the initial conditions for Test 6. Though the HEM is a simplification, the figure illustrates relevant effects which we will discuss in relation to the pressure recordings from the experiments in the following section.

We note the following: the pressure drops closest to the open end first. The depressurization is fast in the single-phase state and there is a discontinuous decrease in wave speed once two-phase flow begins. After this, the flow chokes near the open end, slowing the depressurization down significantly. The decrease of the wave speed once two-phase flow begins causes a short-lasting pressure-plateau to form for the positions further inside the pipe (similar to traffic backing up on a highway), a second long-lasting pressure-plateau forms near the open end when the flow has choked.

5.1.1. Warm experiments, $T_0 \geq 35.8\,°C$

In Figure 8, we present a comparison between the pressure measurements near the open end and the closed end of the pipe for the first 400 ms of depressurization for Test 24 and Test 6. The depressurization paths of these tests pass close to the critical point, with Test 6 passing the closest. We note six events/phenomena which are common to both experiments, and which are marked in Figure 8.

First the rupture disk breaks (1) and a fast pressure drop is recorded. A short pressure plateau is recorded as CO_2 vapor starts forming (2). This is caused by the
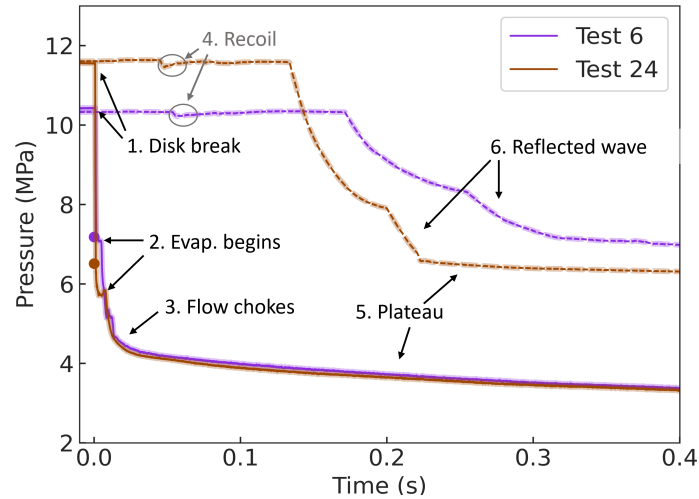
18

Figure 8: Measured pressure at $x = 0.28$ m (solid lines) and $x = 49.98$ m (dashed lines) for Test 6 and Test 24 presented in Table 1. Shaded regions show the 95% confidence interval of the measurements. Circular markers show where the liquid isentrope passes the saturation line for each experiment.

speed of sound decreasing for two-phase flow, an effect which can be reproduced by flow simulations as shown above. After this short plateau, the fast pressure drop continues until the flow chokes at the pipe outlet (3) and a long-lasting pressure plateau is established inside the pipe. Due to the recoil of the pipe[1] at the initial disk rupture, a small pressure perturbation is recorded traveling inwards from the pipe's closed end (4). After approximately 140 ms for Test 24 and 170 ms for Test 6, the rarefaction wave from the disk opening approaches the closed end of the pipe. The rarefaction wave stretches when traveling into the pipe due to the acceleration of the fluid[2]. A pressure plateau is established also here (5). The pressure plateau is reached at a higher pressure near the closed end due to heat transfer and friction in the pipe as shown by Munkejord *et al.* (2020, Fig. 10) using HEM simulations. Finally, the rarefaction wave reaches the closed end of the pipe and is reflected (6).

In addition to these phenomena, Figure 8 shows the points where the liquid depressurization path crosses the saturation line. For Test 6, flashing occurs exactly at the point where the saturation line is crossed, as indicated by the pressure level of the short pressure plateau caused by flashing initiation. Test 6 passes very close to the critical point, as shown in Figure 8. At the critical point, the activation energy for bubble formation vanishes and bubbles form immediately as the saturation line is crossed. For Test 24, there is a pressure undershoot before flashing begins. This is also shown in later simulation results.

---

[1]due to some elasticity in the pipe supports

[2]Theory on rarefaction waves in compressible fluids can be found in, e.g., Toro (2009, Chap. 4)
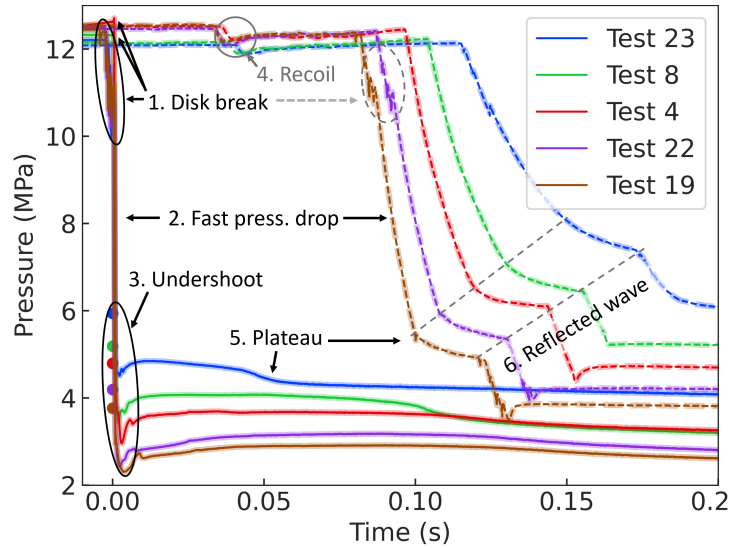
Figure 9: Measured pressure at $x = 0.28$ m (solid lines) and $x = 49.98$ m (dashed lines) for Tests 23, 8, 4, 22 and 19 presented in Table 1. Shaded regions show the 95% confidence interval of the measurements. Circular markers show where the liquid isentrope passes the saturation line for each experiment.

5.1.2. Cold experiments, $10.2\,°C \leq T_0 \leq 31.5\,°C$

In Figure 9, we present a comparison between the resulting pressure measurements near the open end and the closed end of the pipe for the first 200 ms of depressurization for Tests 4, 8, 19, 22 and 23. Six phenomena that are common to all these tests are marked in the figure. These are nearly all the same as for the warm experiments, with the exception of a clear pressure undershoot and recovery.

First, the rupture disk breaks (1). For the multilayered rupture disk, there are several rapid pressure drops as each layer breaks, creating jagged pressure waves. The disk break is followed by a fast pressure drop (2). For all the tests presented in Figure 9, the CO_2 is in a liquid state initially and the pressure waves travel very fast. After the initial pressure drop, there is a pressure undershoot (3) and a recovery when gas bubbles suddenly form. Due to the recoil of the pipe at the initial disk rupture, a pressure perturbation is recorded traveling from the closed end of the pipe (4). At the open end, the flow chokes at the pipe outlet shortly after the pressure recovery and a pressure plateau is formed inside the pipe (5).

After 70 ms to 120 ms, the rarefaction wave from the disk opening approaches the end of the pipe. The pressure wave has stretched when traveling into the pipe. A pressure plateau is established also here (5). Finally, the rarefaction wave reaches the closed end of the pipe and is reflected (6). For Tests 19 and 22, pressure disturbances from the opening of the multilayered disk can be seen in the reflected wave. A slight pressure-undershoot is observed after the reflected wave and a somewhat lower plateau pressure is established.

The comparison of the cold experiments in Figure 9 show many interesting

20

trends. We will here focus on three main observations: how the initial temperature affects the pressure waves and plateaus, the non-equilibrium effects and finally the presence of "humps" in the pressure paths.

Pressure wave and plateau. Figure 9 shows clear trends regarding how the initial temperature affects the pressure paths of the experiments. The plateau pressure decreases for the depressurization tests with lower initial temperature. This is reasonable as the saturation pressure of CO_2 decreases with temperature. We can also observe that the single-phase wave speed in the CO_2 is slower for the warm experiments and faster for the colder ones as the rarefaction wave arrives later at the position $x = 49.98$ m for the warmer experiments. This is also in agreement with theory as pressure waves travel faster in denser fluids and the initial density of the colder experiments is higher than for the warmer experiments.

Non-equilibrium effects. The cold tests show a clear pressure undershoot and recovery, which are signs of non-equilibrium phase change in the flow. It has been shown by several authors that the pressure undershoot and recovery cannot be described by equilibrium flow models, e.g., (Winters and Merte, 1979; Deligiannis and Cleaver, 1990; Barták, 1990; Ivashnyov *et al.*, 2000; Munkejord *et al.*, 2020). We also demonstrate this in Section 5.2.1. For the cold tests, there is a significant distance between the pressure where the depressurization path passes the saturation line and where it reaches the liquid limit of metastability, as shown in Figure 2. This allows for delayed gas formation. The delayed phase change causes the pressure recovery as bubbles are suddenly formed and grow violently. Once phase change is initiated, the speed of sound decreases and the flow chokes shortly afterwards, causing the long-lasting pressure plateau to form.

Pressure humps. An interesting phenomenon, which can be better observed in Figure 10, is the presence of a pressure "hump" in the pressure traces measured near the open end of the pipe. Following the pressure undershoot, the pressure rebounds and stays high for a few ms before the pressure again begins to decrease, though much slower than before. For the higher-temperature experiments, the pressure hump is more pronounced and lasts for a shorter amount of time. This phenomenon is observed for all the cold experiments, despite varying initial temperatures and the application of different rupture disks. The same effect can also be observed in the results of Botros *et al.* (2016) and the water depressurization experiments of Edwards and O'Brien (1970).

Ivashnyov *et al.* (2000) were able to reproduce similar pressure traces for the Edwards and O'Brien (1970) pipe blowdown experiments by accounting for bubble transport, growth, and bubble breakup near the open end of the pipe. They argue that the breakup of bubbles near the open end of the pipe provides more available surface area for bubble growth to occur, and the violent bubble growth causes an elevated pressure to be sustained for a short amount of time. Provided that bubble growth and breakup causes the pressure hump, the hump likely ends once the flow transitions away from the bubbly flow regime.

In order to gain a better understanding of the non-equilibrium effects observed in the experimental campaign, and to evaluate the accuracy of the HRM*, we compare
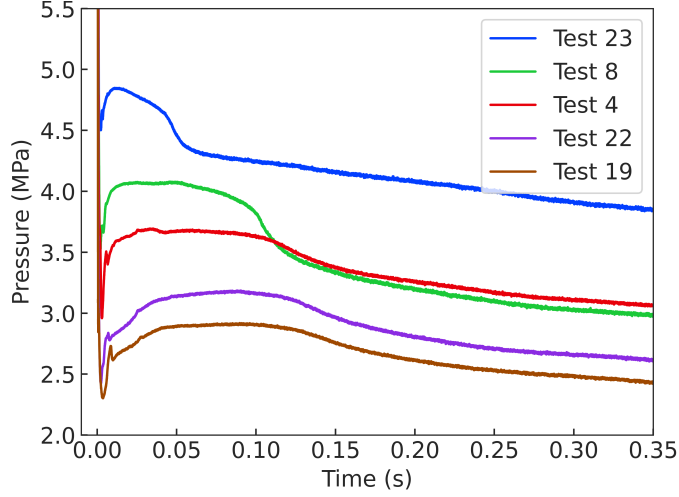
Figure 10: Measured pressure at $x = 0.28\,\text{m}$ for Tests 4, 8, 19, 22 and 23, zoomed in to show the pressure "hump" which follows the pressure undershoot and recovery.

the experimental results to computational fluid dynamics simulations using the HRM* and the HEM as described in Sections 3 and 4.

5.2. Analysis of 1D CFD models and comparison to experiments

In this section, the results of the numerical simulations are presented and compared to the experimental results. For all the numerical simulations, a Courant–Friedrichs–Lewy (CFL) number of 0.9 is applied[3]. The 1D simulation domain is 61.7 m long. Based on a grid-refinement study presented in Appendix B, 10,000 grid cells are employed in all the simulations.

The section is structured as follows. First a study on the effect of the relaxation time in the simulations is presented and appropriate relaxation times are chosen for the conditions of each depressurization test. Next, we compare the simulated and measured pressure in the pipe for all the experiments. Finally, more detailed analysis is conducted to study the speed of the flashing front and how the flow deviates from the saturation line. Here, we refer to the flashing front as the location in the pipe where the flow transitions from single-phase liquid flow to two-phase gas-liquid flow due to flashing.

5.2.1. The relaxation time in the HRM*

For the HRM*, a relaxation time, θ, must be chosen in order to estimate the mass-transfer rate between the phases. Here, we study how the choice of this relaxation time, θ, affects the simulated pressure evolution during depressurization. The effect of θ is studied for initial conditions corresponding to Test 19 up to $t_{\text{end}} = 40\,\text{ms}$.

---

[3]For the present numerical solver, the CFL number must be between 0 and 1 to ensure stability (LeVeque, 2002, Ch. 4.4).

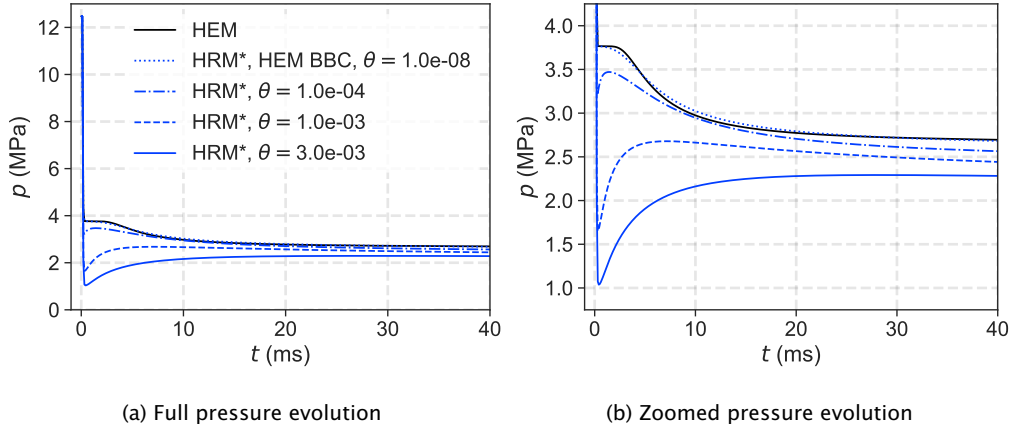(a) Full pressure evolution   (b) Zoomed pressure evolution

Figure 11: Comparison between HRM* with various relaxation times θ and HEM at $x = 0.08\,\mathrm{m}$ for the initial conditions of Test 19.

Test 19 was chosen as the liquid depressurization path does not cross the liquid spinodal, such that the effect of long relaxation times can be tested without the simulation reaching thermodynamically unstable states. Based on the findings, we choose appropriate relaxation times for the experiments studied.

Figure 11 shows the pressure evolution 8 cm from the open end of the pipe for the HRM* with three different relaxation times in the range from 0.1 ms to 3 ms. The results are compared to those of the HEM. We also illustrate how the HRM* relaxes towards HEM by enforcing the HEM BBC and setting $\theta = 10\,\mathrm{ns}$. The relaxation time has a clear effect on the pressure undershoot and recovery, and the pressure undershoot is larger for longer relaxation times. However, after approximately 20 ms, the pressure predicted by HRM* converges to a value somewhat below that calculated using HEM. For $\theta = 0.1\,\mathrm{ms}$, this pressure is closer to the HEM pressure than for the longer relaxation times. However, the difference is small, only 0.1 MPa–0.2 MPa.

When the HEM BC is enforced and $\theta = 10\,\mathrm{ns}$, the pressure prediction of the HRM* nearly overlaps with the HEM's pressure, though some numerical dissipation is present from the calculation of the strong mass transfer. With the present mass-transfer model, the boundary condition must be changed in order to obtain larger differences in the resulting pressure plateau near the open end of the pipe. The present BC for HRM* assumes the lowest possible choking pressure for a given entropy and mass fraction to not disturb the predicted non-equilibrium effects. Enforcing a higher choking pressure in the BC would lead to a higher plateau pressure, but it may also limit the predicted pressure undershoot.

We note three findings from this initial study:

1. Longer relaxation times provide larger pressure undershoots.

2. Before approximately 20 ms, the choice of relaxation time for the HRM* has a large effect on the simulated pressure near the pipe outlet.

3. After approximately 20 ms, the pressure calculated by HRM* near the pipe

Table 2: Chosen relaxation time for HRM* for each experiment, listed in the order of descending initial temperature.

Test no.	p_0 (MPa)	T_0 (℃)	θ (ms)
6	10.40	40.0	0.04
24	11.56	35.8	0.14
23	12.19	31.5	0.55
8	12.22	24.6	1.10
4	12.54	21.1	1.50
22	12.48	14.9	2.00
19	12.47	10.2	2.50

(a) The relaxation time as a function of initial temperature, T_0.

(b) The relaxation time as a function of the scaled, relative initial entropy, $\Delta \tilde{s}_0 = \dfrac{s_0 - s_c}{s_{\text{tr.}} - s_c}$.
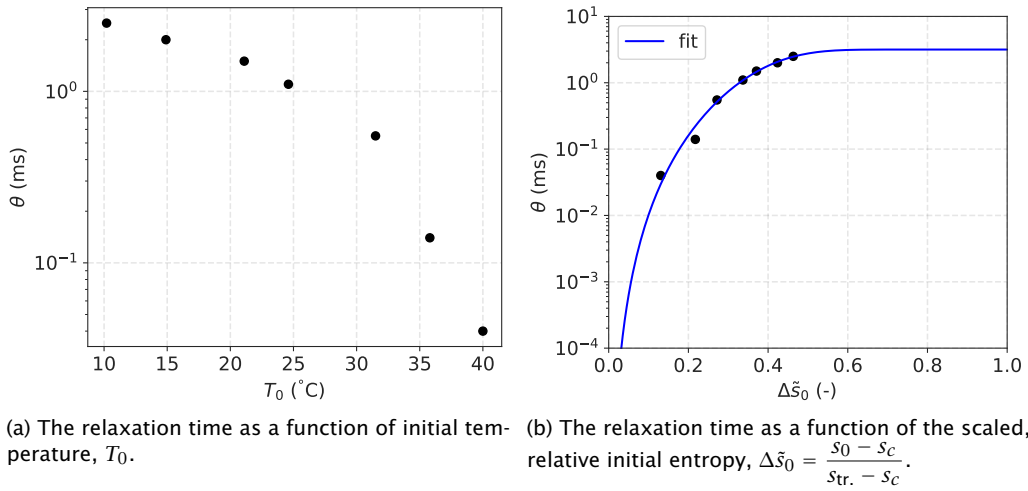
Figure 12: The chosen relaxation times for HRM* plotted with the proposed relaxation time correlation.

outlet converges towards a value below that calculated by HEM. This plateau pressure could be increased by applying a different BC, but a different BC may also limit the obtained pressure undershoot.

Based on these findings, θ was chosen by visual inspection to provide the best possible fit of the calculated pressure evolution to the pressure dip measured by the sensors near the open end of the pipe (PT201–PT203), 8 cm to 28 cm from the open end. Relaxation times in the range from 0.01 ms to 4 ms were tested. The chosen relaxation time for each experiment is displayed in Table 2.

It is clear that the higher-temperature experiments have a much shorter relaxation time than the colder ones. The relaxation time of the coldest experiment is approximately 60 times longer than for the warmest experiment. In Figure 12a, the chosen relaxation time is plotted as a function of the initial temperature for each depressurization test. For the higher temperatures, $T_0 \geq 31.5\,°C$, there is a logarithmic decrease in the relaxation time for increasing temperatures. For the colder tests, the relaxation time increases linearly for increasing temperatures. Obviously, there is

no "optimal" relaxation time which can be applied for all the different cases as the phase-change process varies drastically for the different initial temperatures.

At the critical point, the energy barrier for creating a bubble vanishes, so the relaxation time should be zero. Our chosen relaxation times fitting the experimentally measured pressure undershoot further appears to approach a constant value at colder temperatures, or lower entropies. Based on this information, we propose the following correlation for the relaxation time for different depressurization paths:

$$\theta = a \left[1 - \exp\left(-b \Delta \tilde{s}_0^c\right) \right], \tag{32}$$

where

$$\Delta \tilde{s}_0 = \frac{s_0 - s_c}{s_{\mathrm{tr.}} - s_c}, \tag{33}$$

is the scaled, relative initial entropy and s_0 is the initial entropy before the depressurization begins, s_c is the critical point entropy and $s_{\mathrm{tr.}}$ is the triple point entropy. Note that $\Delta \tilde{s}_0 = 0$ when $s_0 = s_c$ and $\Delta \tilde{s}_0 = 1$ when $s_0 = s_{\mathrm{tr.}}$. As the depressurization path is expected to be nearly isentropic before phase change begins, the scaled, relative initial entropy provides information on whether the depressurization path will cross the saturation line closer to the triple point or the critical point. We find the best fit for our chosen relaxation times with $a = 3.165\,\mathrm{ms}$, $b = 33.283$ and $c = 4.014$. The resulting correlation is shown in Figure 12b. Near $\Delta \tilde{s}_0 = 0$, the relaxation time goes to zero and for $\Delta \tilde{s}_0 \lesssim 0.5$ the relaxation time becomes constant, equal to $3.165\,\mathrm{ms}$. More experimental data are needed to determine whether this functional form is appropriate for the relaxation time. The correlation may also be tested for different fluids.

5.2.2. Comparison to experiments

In this section, we compare HEM and HRM* simulations to experimental data. The simulations are run up to $t_{\mathrm{end}} = 100\,\mathrm{ms}$. As the non-equilibrium effects are most pronounced near the pipe outlet, we present the results for the simulated and measured pressure at the sensor closest to the pipe outlet, PT201, which is situated 8 cm from the open end. For plots over time, the plotted line width of the experimental measurement is chosen to match the 95% confidence interval of the data. Thus if the model predictions do not overlap with the line, they are outside of the experimental uncertainty. We also study the pressure wave along the length of the pipe. Once again, we separate the warm (6 and 24) and cold (4, 8, 19, 22, 23) tests and discuss them separately.

Warm experiments, $T_0 \geq 35.8\,°\mathrm{C}$. In Figure 13, the modeled and measured pressure traces at 8 cm from the open end of the pipe are shown for Test 6 and Test 24 up to $t = 15\,\mathrm{ms}$. The flashing begins for both tests at a very short pressure plateau after about 1 ms and the flow chokes at the pipe outlet after approximately 10 ms. The difference between HEM and HRM* is small for Test 6, and more pronounced for Test 24.

For Test 24, flashing begins at a lower pressure than what is predicted by HEM. The HEM predicts flashing at approximately 6.5 MPa, at the point where the single-phase isentrope crosses the saturation line. However, at 1 ms to 3 ms, the experimental
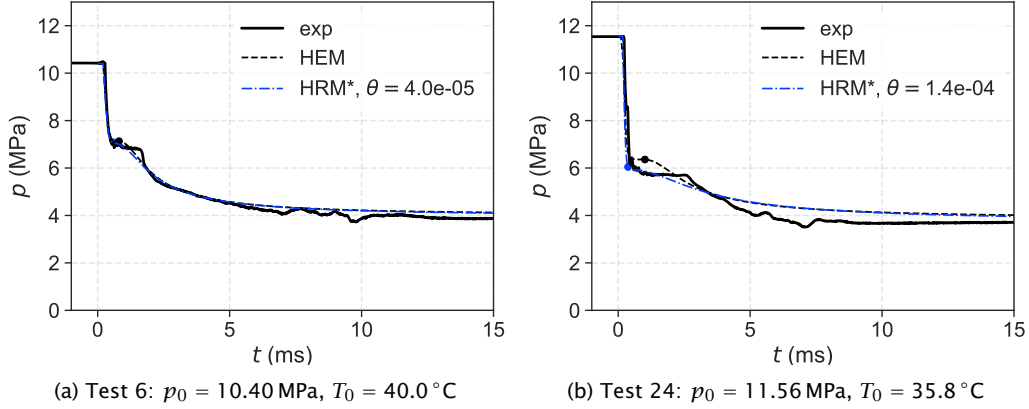
(a) Test 6: $p_0 = 10.40$ MPa, $T_0 = 40.0\,°C$ (b) Test 24: $p_0 = 11.56$ MPa, $T_0 = 35.8\,°C$

Figure 13: Measured (full lines) and simulated pressure (dashed lines) at $x = 0.08$ m from the open end for Tests 6 and 24. Markers show where $x_g > 0.001$ for the simulations, illustrating where two-phase flow begins.

measurements show a pressure plateau around $p = 5.8$ MPa, indicating boiling. The HRM* agrees with the delayed boiling, but it does not obtain a pronounced pressure plateau as observed in the experimental measurement. The HEM obtains a sharper pressure plateau than HRM*. As shown in Figure 7, the plateau is related to the decrease in speed of sound once flashing begins. Though HRM* is fitted to the approximate flashing onset, the mass-transfer rate is too low to provide the abrupt decrease in the speed of sound that causes the plateau. However, the prediction of the pressure plateau may also be affected by numerical dissipation, causing an unwanted smoothing effect. After the onset of flashing, the models obtain a too slow pressure drop. Finally, both HEM and HRM* overestimate the pressure plateau after choking occurs.

In Figure 14, we show the measured and simulated pressure wave along the pipe at $t = 100$ ms. The predictions of the HEM and HRM* models are overlapping and they agree well with the experimental data. The rarefaction wave is split into two waves along the pipe. Closest to the open end of the pipe, there is a slow-moving two-phase rarefaction wave, and further inside the pipe there is a fast-moving single-phase rarefaction wave. In-between these two waves is a plateau where the CO_2 is in the single phase. If no friction or heat transfer was present, this plateau would be at a constant pressure, at the pressure where flashing begins. The heat transfer from the steel wall of the pipe to the fluid and the friction in the pipe cause a slope in the pressure plateau so that the pressure stays above the boiling pressure.

Cold experiments, $10.2\,°C \le T_0 \le 31.5\,°C.$ In Figure 15, the simulated and measured pressures at 8 cm from the open end of the pipe are shown for Tests 4, 8, 19, 22 and 23. For these tests, the difference between HEM and HRM* is substantial, particularly during the first 10 ms of the flow. As expected, HEM reaches two-phase flow too early, and does not capture the pressure undershoot and recovery. At $t \approx 1$ ms, the difference between the pressure calculated using the HEM and the recorded pressure is in the order of 2 MPa for Tests 8, 19, 22 and 23. After the first few ms of the

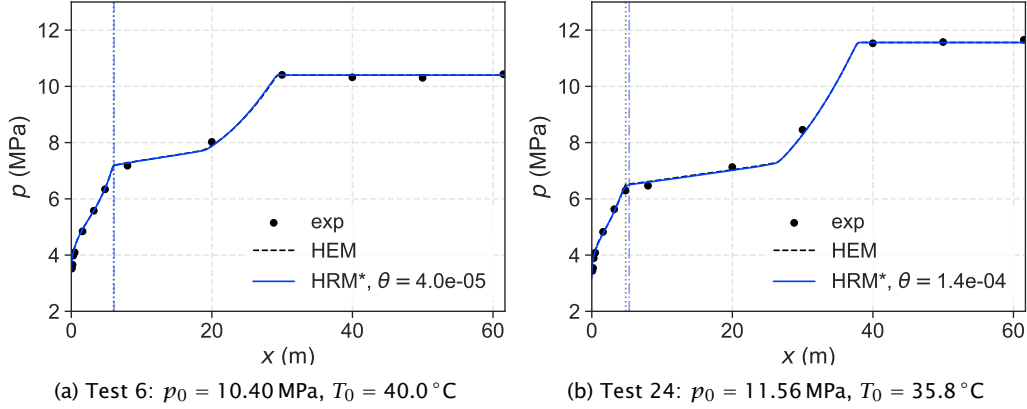(a) Test 6: $p_0 = 10.40$ MPa, $T_0 = 40.0\,^{\circ}$C

(b) Test 24: $p_0 = 11.56$ MPa, $T_0 = 35.8\,^{\circ}$C

Figure 14: Measured and simulated pressure along the pipe at $t = 100$ ms. The vertical lines mark where two-phase flow begins near the open end for HEM (dotted line) and HRM* (dash dotted line).

simulations, there is a transition from HEM overestimating the pressure to HEM *under*estimating the pressure for Tests 4, 8 and 23. This also occurs for Tests 19 and 22 for a longer t_{end}.

HRM* clearly outperforms HEM for the first ms as it captures a pressure undershoot and recovery recorded 8 cm from the open end. Figure 15c shows that Test 4 does not obtain a clear pressure undershoot and recovery at this position, causing a discrepancy between the HRM* pressure and the experimental measurements. However, as shown in Figure 9, a pressure undershoot and recovery is observed for Test 4 at 28 cm from the open end. The difference between the recorded pressure behaviors 8 cm and 28 cm from the open end for this case is larger than the measurement uncertainty. The result may simply reflect the chaotic nature of the flow during the first few ms of the depressurization and it might not be possible to fully capture this with a 1D model. The pressure recovery calculated by the HRM* is a bit more abrupt than the experimental measurements. This is particularly evident for Test 8. After the pressure recovery, HRM* also underestimates the pressure for Tests 4, 8 and 23, and a pressure plateau is established somewhat below that of HEM.

As discussed in Section 5.1, the presence of pressure humps for the colder experiments suggests a violent bubble breakup and growth process (Ivashnyov *et al.*, 2000). It is the elevated pressure hump that neither HEM nor HRM* can capture, causing an underestimation of the pressure over time. The underestimation of the HEM can be very clearly seen in Munkejord *et al.* (2020, Fig. 11), where longer simulations were conducted. In order to capture the boiling process fully, a physics-based model for the mass-transfer rate would be needed, where bubble growth and breakup is accounted for.

We now consider the depressurization wave along the pipe. In Figure 16 we show the simulated and measured pressure wave along the pipe at $t = 100$ ms for all the cold experiments. Generally, the models provide quite similar predictions and agree well with the measured pressure data along the pipe. The clearest difference in the model predictions is at the beginning of the two-phase rarefaction wave at around
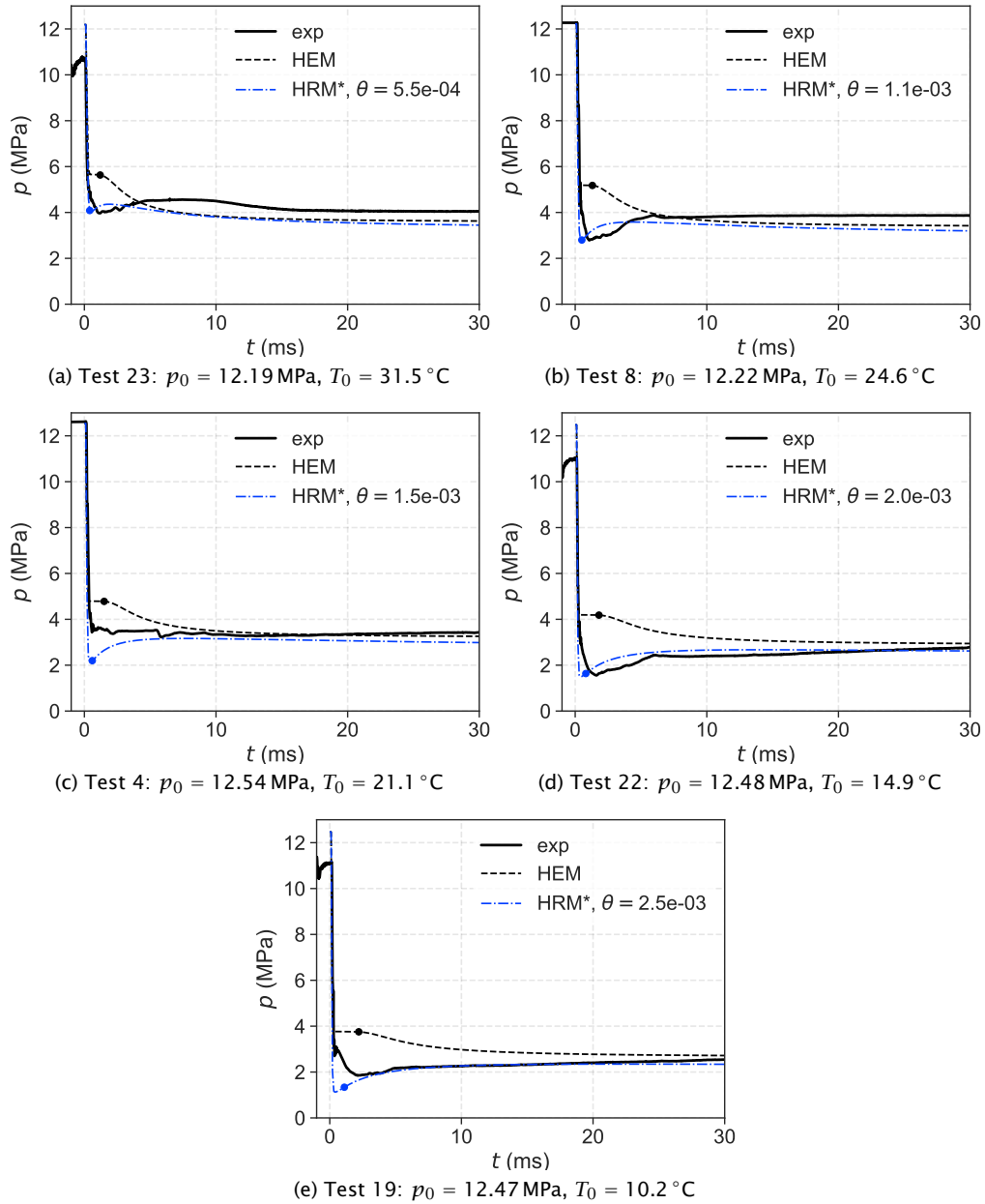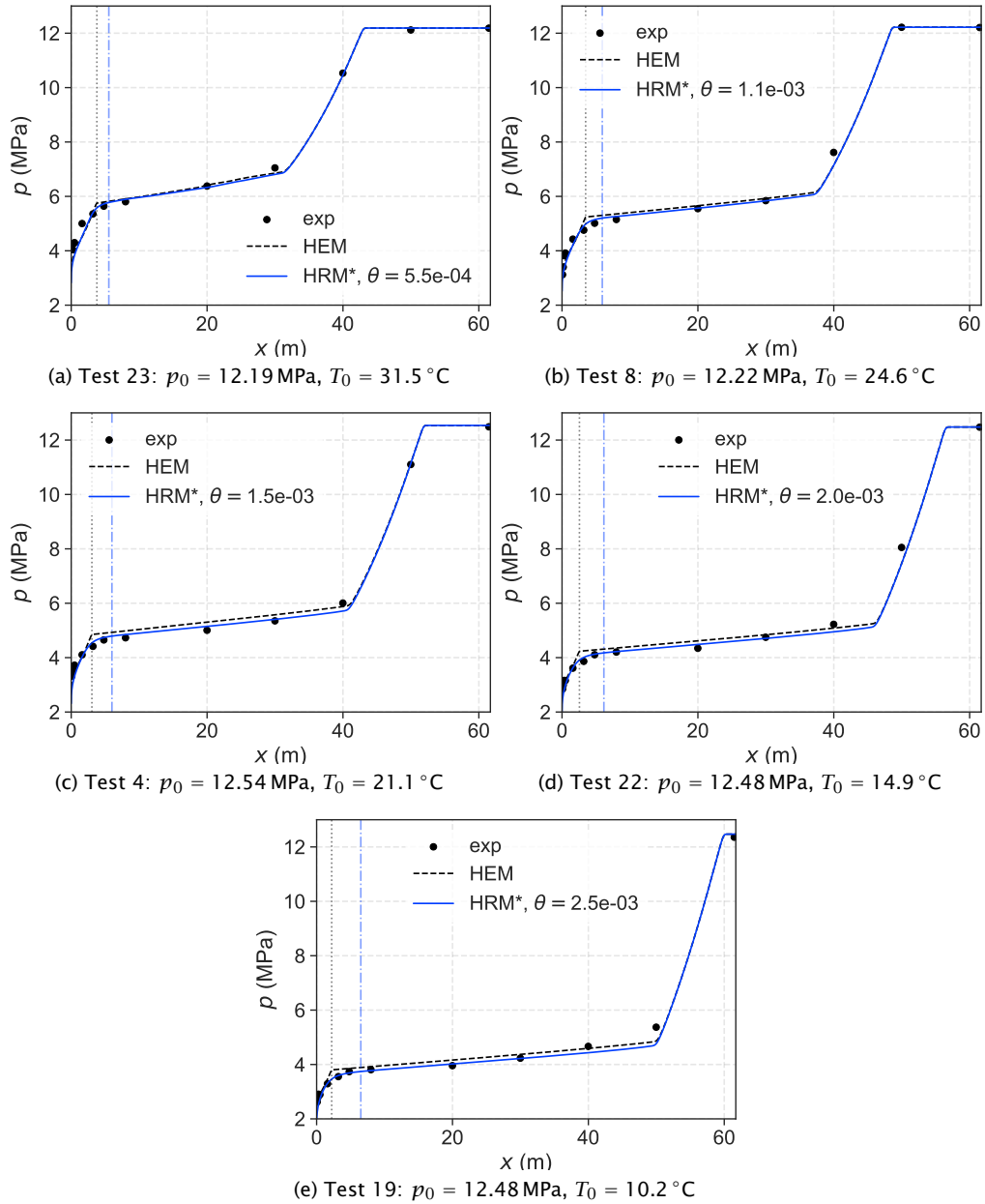
27

(a) Test 23: $p_0 = 12.19\,\text{MPa}$, $T_0 = 31.5\,^\circ\text{C}$

(b) Test 8: $p_0 = 12.22\,\text{MPa}$, $T_0 = 24.6\,^\circ\text{C}$

(c) Test 4: $p_0 = 12.54\,\text{MPa}$, $T_0 = 21.1\,^\circ\text{C}$

(d) Test 22: $p_0 = 12.48\,\text{MPa}$, $T_0 = 14.9\,^\circ\text{C}$

(e) Test 19: $p_0 = 12.47\,\text{MPa}$, $T_0 = 10.2\,^\circ\text{C}$

Figure 15: Measured (full lines) and simulated pressure (dashed lines) at $x = 0.08\,\text{m}$ from the open end for Tests 4, 8, 19, 22 and 23. Markers show where $x_g > 0.001$ for the simulations, illustrating where two-phase flow begins.

(a) Test 23: $p_0 = 12.19\,\mathrm{MPa}$, $T_0 = 31.5\,^\circ\mathrm{C}$

(b) Test 8: $p_0 = 12.22\,\mathrm{MPa}$, $T_0 = 24.6\,^\circ\mathrm{C}$

(c) Test 4: $p_0 = 12.54\,\mathrm{MPa}$, $T_0 = 21.1\,^\circ\mathrm{C}$

(d) Test 22: $p_0 = 12.48\,\mathrm{MPa}$, $T_0 = 14.9\,^\circ\mathrm{C}$

(e) Test 19: $p_0 = 12.48\,\mathrm{MPa}$, $T_0 = 10.2\,^\circ\mathrm{C}$

Figure 16: Measured and simulated pressure along the pipe at $t = 100\,\mathrm{ms}$. The vertical lines mark where two-phase flow begins near the open end for HEM (dotted line) and HRM* (dash dotted line).

$x = 5$ m, where HEM predicts a sharper change in the pressure than HRM* where two-phase flow begins. This difference is caused by the relaxation time in HRM* giving a more gradual flashing process. The experimental data agree more with the HRM* prediction in this region of the pipe. For the two warmer tests, Test 23 with $T_0 = 31.5\,°C$ and Test 8 with $T_0 = 24.6\,°C$, the predictions of HEM and HRM* are nearly overlapping otherwise.

For the three coldest tests, HRM* predicts a slightly lower pressure than HEM in-between the single-phase and two-phase rarefaction waves. Around 10 m to 40 m from the open end of the pipe, the experimental measurements seem to agree more with the prediction of HRM*, whereas further inside the pipe behind the single-phase rarefaction wave, the experimental measurements seem to agree more with HEM. It is possible that the friction and/or the heat transfer models should be slightly stronger, providing a larger slope in the pressure along the pipe between the two-phase and single-phase rarefaction waves. The HRM* would then agree better with the measured data.

5.3. Analysis of model predictions and experimental non-equilibrium effects

5.3.1. Flashing front

Recent visualization experiments for the depressurization of CO_2 conducted by Quinn *et al.* (2022) show that the flashing front travels faster than what is predicted by HEM. We study the simulated flashing front by plotting the volume fraction of gas along the pipe at various times. In Figure 17, we show the simulated volume fraction of gas along the pipe at times $t = 2$ ms, $t = 4$ ms and $t = 6$ ms for Test 8. The plots show that the flashing front predicted by HRM* moves faster into the pipe than that of HEM. This is also the case for the other depressurization tests. HRM* predicts a slightly lower pressure plateau than HEM and a more gradual transition from single-phase to two-phase flow due to the relaxation time in the flashing process. As flashing begins in all grid cells where the pressure is below the saturation pressure, flashing is initiated faster, further inside the computational domain for HRM*. Furthermore, following the subcharacteristic condition (see, e.g., Flåtten and Lund (2011)), the two-phase mixture speed of sound is higher for HRM* than for HEM, such that the pressure drops faster in the two-phase region, also bringing more grid cells to a low enough pressure to initiate flashing. These two effects cause the flashing front to move faster into the pipe for HRM*, providing qualitative agreement with the experimental observations of Quinn *et al.* (2022).

5.3.2. Superheat and pressure undershoot

In order to gain further understanding on the non-equilibrium effects observed in the experiments, we plot the predicted depressurization path of the HRM* in a *p-T* diagram for all the experiments 8 cm from the open end, as shown in Figure 18. We cannot compare these *p-T* paths directly to experimental data due to the response time of the temperature sensors. The homogeneous superheat limit (SHL) predicted by classical nucleation theory is also included in the plot. This illustrates the line where a rate of 10^{12} bubbles $m^{-3}\,s^{-1}$ are predicted to nucleate homogeneously in the fluid, i.e. through random density fluctuations in the fluid. It has been shown by Wilhelmsen and Aasen (2022) that the maximum superheat attained in nozzle
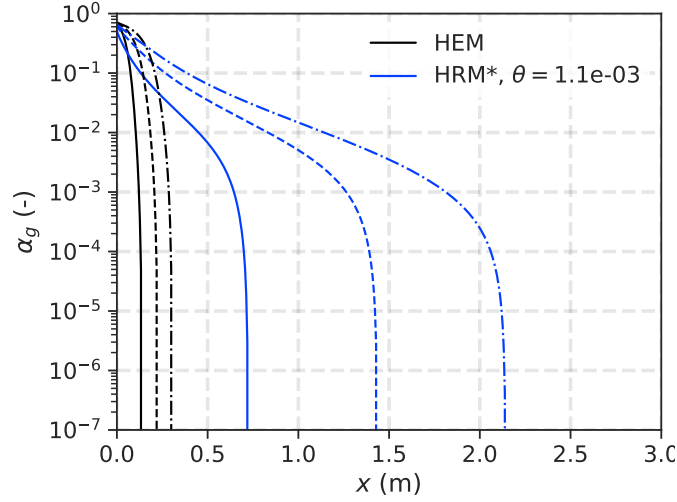
Figure 17: Evolution of the gas volume fraction along the pipe for Test 8 calculated using the HEM (black lines) and HRM* (blue lines) for $t = 2\,\text{ms}$ (full lines), $4\,\text{ms}$ (dashed lines) and $6\,\text{ms}$ (dash dotted lines).

flow can be predicted by the homogeneous SHL for warm temperatures. Preliminary studies of the presented data shows a similar trend for pipe depressurizations (Log *et al.*, 2022). Details on how the homogeneous SHL can be computed are provided in Appendix A. Note that even though the homogeneous SHL can predict the maximum degree of superheat observed in warm experiments, this does not mean that heterogeneous nucleation, i.e., nucleation occurring on a surface such as the wall of the pipe, is not present.

The HRM* simulations indicate strong non-equilibrium. Nevertheless, we would not expect the state of the CO_2 in the pipe to pass beyond the homogeneous SHL. For the colder experiments, the HRM* yields large pressure undershoots and strong superheating, indicating strong non-equilibrium effects. The *p-T* paths of Tests 23, 8, 4 and 22 calculated by the HRM* pass beyond the homogeneous SHL and approach the liquid spinodal. It is possible to reach such degrees of superheat, but we find it unlikely that they should be reached in pipe depressurization experiments. Instead the temperature is most likely colder at the lowest point of the pressure dip than what is predicted by the HRM*, reducing the degree of superheat reached. In other words, we hypothesize that the depressurization paths will move further to the left in the phase diagram than what is predicted by HRM*. Such a cooling effect occurs when two-phase liquid-gas flow begins.

The above analysis suggests that the HRM* mass-transfer rate should be somewhat higher, producing more vapor once the saturation line is passed – and in particular when the superheat limit is passed. This could be achieved by reducing the relaxation time for increasing superheat. After all, the relaxation time is likely not constant. More physics should be incorporated in the mass-transfer rate model to account for this effect.
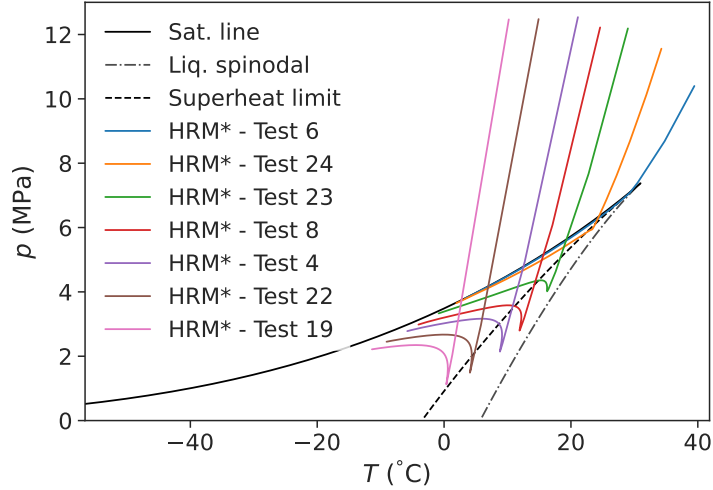
31

Figure 18: The p-T paths simulated by the HRM* at $x = 8\,\text{cm}$ from the open end of the pipe.

In Appendix C we test whether the high superheat predicted by the HRM* is caused by our minimum BBC. The minimum BBC intentionally allows for large superheat and pressure undershoots. However, we find that applying a BC with earlier choking does not change the superheat reached in the model, provided that the relaxation time is re-fitted to match the observed pressure undershoot. Thus, the problem lies with the mass-transfer model: it cannot fit the pressure undershoot without providing a too strong superheat. For the interested reader, the simulated p-T-path in the first grid cell in the computational domain, and in the outflow boundary cell for the HRM* is shown in Appendix D.

5.3.3. Onset of flashing

Based on the depressurization paths of our non-equilibrium simulations, we assume that in the HRM*, more vapor should be produced before the bottom of the pressure dip is reached. We here present an analysis of the vapor production in the experiments and for the HRM*. This is done by studying the experimental and simulated pressure over a short time-frame of 10 ms and observing signs of bubble nucleation, namely:

- pressure disturbances, and

- reduction in the depressurization rate.

In Figure 19, we show the recorded and simulated pressure path at 8 cm from the open end of the pipe for the five warmest experiments, Test 4, 6, 8, 23 and 24. The pressure where the liquid isentrope crosses the homogeneous superheat limit (SHL) is marked by a red cross. The pressure where a significant mass fraction of gas is detected for the HRM* simulation, $x_g > 0.001$, is marked with a circle. For all these experiments, we observe the signs of bubble nucleation for the experimental measurement near the point where the superheat limit is crossed. For the warmest

32

experiments, Tests 6, 23 and 24, bubble nucleation appears to occur at a pressure slightly below the superheat limit. For Test 8, bubble nucleation appears to occur slightly above the superheat limit. Interestingly, the pressure plateau recorded for Test 4 matches exactly with the superheat limit. For the HRM*, significant vapor production occurs at a lower pressure. Though the lowest point of the pressure dip matches well with the experiments, the details of the phase change is not fully captured by the HRM*.

In Figure 20, we show the recorded and simulated pressure path at 8 cm from the open end of the pipe for the two coldest experiments, Test 19 and Test 22. We once again observe signs of significant vapor production in the recorded pressure at a higher pressure than what is predicted by the HRM*. In contrast to the warmer experiments, bubble nucleation for Test 19 and Test 22 occurs far above the homogeneous superheat limit. In fact, the pressure of Test 19 never reaches the expected homogeneous superheat limit, and therefore no red cross is marked in Figure 20b. For these cold initial temperatures, the maximum degree of superheat is likely determined by heterogeneous nucleation instead of homogeneous nucleation. This transition occurs somewhere between the initial conditions of Test 4 and Test 22, i.e., $14.9\,°C \leq T_0 \leq 21.1\,°C$ and $p_0 \approx 12\,MPa$.

6. Conclusion

In the present work, we have presented a series of CO_2 depressurization experiments and compared the pressure measurements of the first 100 ms with model predictions of a simple non-equilibrium relaxation model (HRM*) and the homogeneous equilibrium model (HEM). This is done in order to better understand and quantify non-equilibrium effects during the flashing process (boiling caused by the depressurization). The non-equilibrium phase-transition is characterized by a pressure undershoot and recovery. This is important to take into account in engineering tools to accurately estimate mass flow rates through valves and orifices, and for safety assessments such as the prediction of running ductile fracture in CO_2-carrying pipelines.

The CO_2 depressurization tests are conducted at seven different initial temperatures for an initial pressure of approximately 12 MPa. For the two warmest experiments, where the depressurization paths pass very close to the critical point of CO_2, no pressure recovery was observed. Our simulations indicate that the phase change occurred slightly out of equilibrium. For the lower temperature experiments, a clear pressure undershoot and recovery was observed near the pipe outlet. The models suggest strong non-equilibrium effects.

The HRM* was fitted to the experimentally measured pressure dip by tuning a relaxation time. The relaxation time decreases for increasing initial temperatures, with the relaxation time for the coldest test at $T_0 = 10.2\,°C$ being approximately 60 times longer than that for the warmest test at $T_0 = 40.0\,°C$. We suggest a correlation for the relaxation time based on the initial entropy of the fluid in the pipe, where the relaxation time goes to zero at the critical point entropy. This is in agreement with bubble nucleation theory. More experimental data are needed to determine the accuracy of the correlation at colder temperatures, with $T_0 \leq 10\,°C$, and different initial pressures. The pressure-temperature paths simulated by the HRM* near the

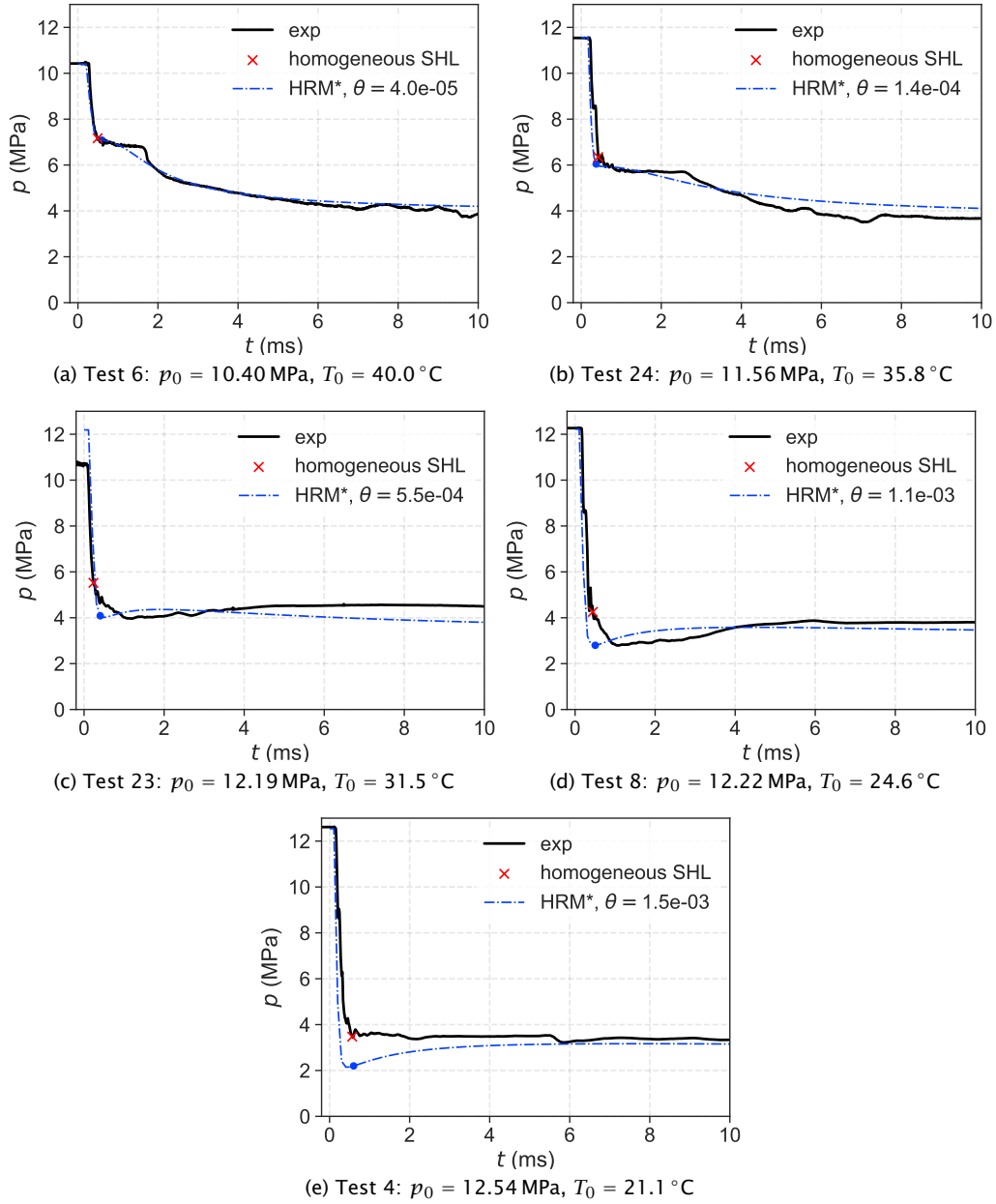(a) Test 6: $p_0 = 10.40\,\text{MPa}$, $T_0 = 40.0\,^\circ\text{C}$

(b) Test 24: $p_0 = 11.56\,\text{MPa}$, $T_0 = 35.8\,^\circ\text{C}$

(c) Test 23: $p_0 = 12.19\,\text{MPa}$, $T_0 = 31.5\,^\circ\text{C}$

(d) Test 8: $p_0 = 12.22\,\text{MPa}$, $T_0 = 24.6\,^\circ\text{C}$

(e) Test 4: $p_0 = 12.54\,\text{MPa}$, $T_0 = 21.1\,^\circ\text{C}$

Figure 19: Measured and simulated pressure at $x = 0.08\,\text{m}$ from the open end for Tests 4, 6, 8, 23, and 24. The pressure at which the liquid isentrope crosses the homogeneous superheat limit (SHL) is marked as a red cross. A circular markers shows where $x_g > 0.001$ for the HRM* simulations.

34
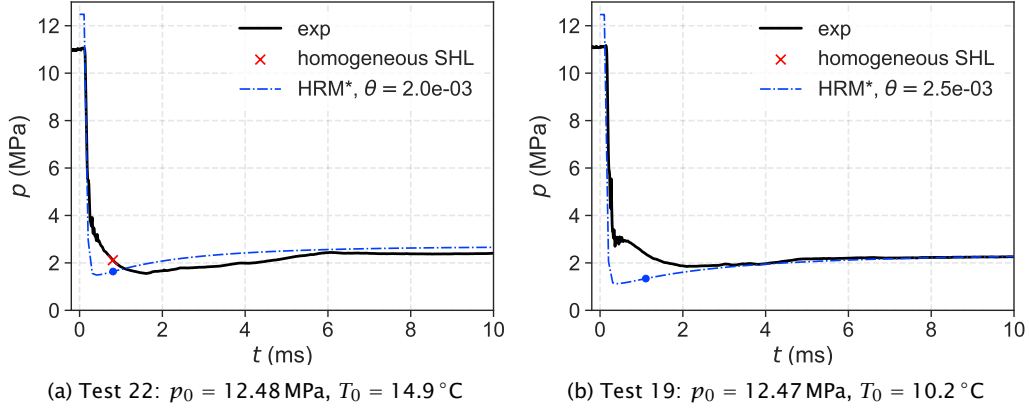
Figure 20: Measured and simulated pressure at $x = 0.08\,\mathrm{m}$ from open end for Test 19 and Test 22. The pressure at which the liquid isentrope crosses the homogeneous superheat limit (SHL) is marked as a red cross. A circular markers shows where $x_g > 0.001$ for the HRM* simulations. For Test 19, the measured pressure always stays above the SHL pressure, so there is no cross marked.

open end of the pipe approach the liquid stability limit (spinodal). Though it is possible to reach the liquid stability limit under extreme conditions, it is unlikely that it is reached in a pipe depressurization experiment. We therefore conclude that the HRM* with the present mass-transfer correlation overestimates the fluid temperature during the first ms of the flow.

Upon closer inspection of the pressure traces near the open end of the pipe, we observe that the onset of significant vapor production predicted by the HRM* occurs at a lower pressure than the point where bubble nucleation is observed in the experiments. The five warmest depressurization tests studied show signs of bubble nucleation near the predicted homogeneous superheat limit. In contrast, the two coldest tests show signs of bubble nucleation at a higher pressure than the homogeneous superheat limit. This is in agreement with the findings of Wilhelmsen and Aasen (2022), showing that the maximum superheat reached becomes determined by heterogeneous nucleation instead of homogeneous nucleation at colder temperatures.

The experimental results show that the pressure remained elevated around 50 ms to 150 ms after the pressure recovery near the pipe outlet for the colder tests, providing a "hump" in the pressure recordings. It is hypothesized that this is caused by bubble breakup and growth enhancing the boiling process and elevating the pressure near the pipe's open end, as suggested by Ivashnyov *et al.* (2000) for water depressurization tests. Both the HEM and the HRM* underestimate the pressure during this time. Finally, the HRM* simulations predict a flashing front that moves faster into the pipe than the HEM simulations. This is in agreement with recent visualization experiments conducted by Quinn *et al.* (2022).

In order to capture the complex non-equilibrium effects during depressurization, a more refined model will be needed for the mass-transfer rate from liquid to gas, incorporating nucleation and bubble growth. A first step in this direction can be

35

to design a relaxation time correlation where the relaxation time decreases as the homogeneous superheat limit is approached. Further work may include the conduction of experiments at different initial pressures and colder initial temperatures. Experiments at colder temperatures are relevant to capture how the non-equilibrium effects change for depressurization paths crossing the saturation line closer to the triple point of CO_2, and to determine the effect of heterogeneous nucleation.

Acknowledgments

Data availability

The experimental data recorded in this study can be downloaded from Zenodo (Log *et al.*, 2023). (The DOI will be activated at publication.)

References

Angielczyk, W., Bartosiewicz, Y., Butrymowicz, D., Seynhaeve, J.-M., Jul. 2010. 1-D modeling of supersonic carbon dioxide two-phase flow through ejector motive nozzle. In: *International Refrigeration and Air Conditioning Conference*. Purdue University. URL https://docs.lib.purdue.edu/iracc/1102/.

Armstrong, K., Allason, D., Oct. 2014. *2" NB shocktube releases of dense phase CO₂*. Tech. rep., GL Noble Denton, Gilsland Cumbria, UK. Available from https://www.dnvgl.com/oilgas/innovation-development/joint-industry-projects/co2pipetrans.html.

Aursand, E., Dumoulin, S., Hammer, M., Lange, H. I., Morin, A., Munkejord, S. T., Nordhagen, H. O., Sep. 2016a. Fracture propagation control in CO_2 pipelines: Validation of a coupled fluid-structure model. *Eng. Struct.* 123, 192–212. doi:10.1016/j.engstruct.2016.05.012.

Aursand, P., Gjennestad, M. A., Aursand, E., Hammer, M., Wilhelmsen, Ø., 2016b. The spinodal of single- and multi-component fluids and its role in the development of modern equations of state. *Fluid Phase Equilib.* 436, 98–112. doi:10.1016/j.fluid.2016.12.018.

Aursand, P., Hammer, M., Lavrov, A., Lund, H., Munkejord, S. T., Torsæter, M., Jul. 2017. Well integrity for CO_2 injection from ships: Simulation of the effect of flow and material parameters on thermal stresses. *Int. J. Greenh. Gas Con.* 62, 130–141. doi:10.1016/j.ijggc.2017.04.007.

Banasiak, K., Hafner, A., 2013. Mathematical modelling of supersonic two-phase R744 flows through converging–diverging nozzles: The effects of phase transition models. *Appl. Therm. Eng.* 51 (1), 635–643. ISSN 1359-4311. doi:10.1016/j.applthermaleng.2012.10.005.

Barták, J., Sep. 1990. A study of the rapid depressurization of hot water and the dynamics of vapour bubble generation in superheated water. *Int. J. Multiphase Flow* 16, 789–798. doi:10.1016/0301-9322(90)90004-3.

Bejan, A., 1993. *Heat Transfer*. John Wiley & Sons, Inc., New York. ISBN 0-471-50290-1.

Bilicki, Z., Kestin, J., Apr. 1990. Physical Aspects of the Relaxation Model in Two-Phase Flow. In: *Proceedings of the Royal Society of London. Series A, Mathematical and Physical Sciences*. Royal Society, vol. 428, pp. 379–397.

Botros, K. K., Geerligs, J., Rothwell, B., Robinson, T., Jun. 2016. Measurements of decompression wave speed in pure carbon dioxide and comparison with predictions by equation of state. *J. Press. Vess. – T. ASME* 138 (3). doi:10.1115/1.4031941.

Botros, K. K., Geerligs, J., Rothwell, B., Robinson, T., Mar. 2017. Effect of argon as the primary impurity in anthropogenic carbon dioxide mixtures on the decompression wave speed. *Can. J. Chem. Eng.* 95 (3), 440–448. doi:10.1002/cjce.22689.

Botros, K. K., Hippert, E., Jr., Craidy, P., Jun. 2013. Measuring decompression wave speed in CO_2 mixtures by a shock tube. *Pipelines International* 16, 22–28.

Brown, S., Beck, J., Mahgerefteh, H., Fraga, E. S., 2013. Global sensitivity analysis of the impact of impurities on CO_2 pipeline failure. *Reliab. Eng. Syst. Safe* 115, 43–54. doi:10.1016/j.ress.2013.02.006.

Brown, S., Martynov, S., Mahgerefteh, H., Chen, S., Zhang, Y., 2014. Modelling the non-equilibrium two-phase flow during depressurisation of CO_2 pipelines. *Int. J. Greenh. Gas Con.* 30, 9–18. doi:10.1016/j.ijggc.2014.08.013.

Clausen, S., Oosterkamp, A., Strøm, K. L., 2012. Depressurization of a 50 km long 24 inches CO_2 pipeline. In: Røkke, N. A., Hägg, M.-B., Mazzetti, M. J. (Eds.), *6th Trondheim Conference on CO2 Capture, Transport and Storage (TCCS-6)*. BIGCCS / SINTEF / NTNU, Energy Procedia vol. 23, Trondheim, Norway, pp. 256–265. doi:10.1016/j.egypro.2012.06.044.

Cosham, A., Eiber, R. J., 29 Sep–03 Oct 2008. Fracture control in carbon dioxide pipelines – The effect of impurities. In: *7th International Pipeline Conference, IPC2008*. ASME, IPTI, Calgary, Canada, vol. 3, pp. 229–240.

Cosham, A., Jones, D. G., Armstrong, K., Allason, D., Barnett, J., 24–28 Sep 2012. Ruptures in gas pipelines, liquid pipelines and dense phase carbon dioxide pipelines. In: *9th International Pipeline Conference, IPC2012*. ASME, IPTI, Calgary, Canada, vol. 3, pp. 465–482. doi:10.1115/IPC2012-90463.

Davis, S. F., Feb. 1988. Simplified second-order godunov-type methods. *SIAM J. Sci. Stat. Comp.* 9, 445–473. doi:10.1137/0909030.

De Lorenzo, M., Lafon, P., Di Matteo, M., Pelanti, M., Seynhaeve, J.-M., Bartosiewicz, Y., 2017. Homogeneous two-phase flow models and accurate steam-water table look-up method for fast transient simulations. *Int. J. Multiphase Flow* 95, 199–219. doi:10.1016/j.ijmultiphaseflow.2017.06.001.

Debenedetti, P. G., 1997. *Metastable Liquids: Concepts and Principles.* Princeton University Press. ISBN 9780691213941. doi:10.1515/9780691213941.

Deligiannis, P., Cleaver, J., 1990. The role of nucleation in the initial phases of a rapid depressurization of a subcooled liquid. *Int. J. Multiphase Flow* 16 (6), 975–984. doi:10.1016/0301-9322(90)90102-O.

Downar-Zapolski, P., Bilicki, Z., Bolle, L., Franco, J., 1996. The non-equilibrium relaxation model for one-dimensional flashing liquid flow. *Int. J. Multiphase Flow* 22 (3), 473–483. doi:10.1016/0301-9322(95)00078-X.

Drescher, M., Varholm, K., Munkejord, S. T., Hammer, M., Held, R., de Koeijer, G., Oct. 2014. Experiments and modelling of two-phase transient flow during pipeline depressurization of CO_2 with various N_2 compositions. In: Dixon, T., Herzog, H., Twinning, S. (Eds.), *GHGT-12 – 12th International Conference on Greenhouse Gas Control Technologies.* University of Texas at Austin / IEAGHGT, Energy Procedia, vol. 63, Austin, Texas, USA, pp. 2448–2457. doi:10.1016/j.egypro.2014.11.267.

ECCSEL, 2021. Depressurization facility. `https://www.eccsel.org/catalogue/113`. Accessed 2023-05-23.

Edwards, A. R., O'Brien, T. P., 1970. Studies of phenomena connected with the depressurization of water reactors. *The Journal of the British Nuclear Energy Society* 9 (2), 125–135.

Einstein, A., 1920. Propagation of Sound in Partly Dissociated Gases. In: *Sitzungsberichte.* Berlin, pp. 380–385. URL `https://einsteinpapers.press.princeton.edu/vol7-doc/373`.

Flåtten, T., Lund, H., Dec. 2011. Relaxation two-phase flow models and the subcharacteristic condition. *Math. Mod. Meth. Appl. S.* 21 (12), 2379–2407. doi:10.1142/S0218202511005775.

Flechas, T., Laboureur, D. M., Glover, C. J., Aug. 2020. A 2-D CFD model for the decompression of carbon dioxide pipelines using the Peng-Robinson and the Span-Wagner equation of state. *Process Saf. Environ.* 140, 299–313. doi:10.1016/j.psep.2020.04.033.

Friedel, L., Jun. 1979. Improved friction pressure drop correlations for horizontal and vertical two phase pipe flow. In: *Proceedings, European Two Phase Flow Group Meeting.* Ispra, Italy. Paper E2.

Gu, S., Li, Y., Teng, L., Wang, C., Hu, Q., Zhang, D., Ye, X., Wang, J., Iglauer, S., May 2019. An experimental study on the flow characteristics during the leakage of high pressure CO_2 pipelines. *Process Saf. Environ.* 125, 92–101. doi:10.1016/j.psep.2019.03.010.

Gungor, K. E., Winterton, R. H. S., Mar. 1987. Simplified general correlation for saturated flow boiling and comparisons of correlations with data. *Chem. Eng. Res. Des.* 65 (2), 148–156.

Guo, X., Yan, X., Yu, J., Yang, Y., Zhang, Y., Chen, S., Mahgerefteh, H., Martynov, S., Collard, A., Jan. 2017.

Pressure responses and phase transitions during the release of high pressure CO_2 from a large-scale pipeline. *Energy* 118, 1066–1078. doi:10.1016/j.energy.2016.10.133.

Hammer, M., Aasen, A., Wilhelmsen, Ø., 2020. Thermopack. `https://github.com/SINTEF/thermopack/`. Accessed 2020-12-15.

Hammer, M., Aasen, A., Wilhelmsen, Ø., 2023. Thermopack. `https://github.com/thermotools/thermopack`. Accessed 2023-06-14.

Hammer, M., Deng, H., Austegard, A., Log, A. M., Munkejord, S. T., Nov. 2022. Experiments and modelling of choked flow of CO_2 in orifices and nozzles. *Int. J. Multiphase Flow* 156, 104201. doi:10.1016/j.ijmultiphaseflow.2022.104201.

Hansen, P. M., Gåthaug, A. V., Bjerketvedt, D., Vågsæther, K., Mar. 2019. Rapid depressurization and phase transition of CO_2 in vertical ducts – small-scale experiments and rankine-hugoniot analyses. *J. Hazard. Mater.* 365, 16–25. doi:10.1016/j.jhazmat.2018.10.092.

Ibrahim, O. M., Hansen, P. M., Bjerketvedt, D., Vågsæther, K., Dec. 2021. Evaporation characteristics during decompression of liquified CO_2 from a conical-shaped vessel. *Results Eng.* 12. doi:10.1016/j.rineng.2021.100304.

IEA, 2021. *Net Zero by 2050 – A Roadmap for the Global Energy Sector.* IEA, Paris. URL `https://www.iea.org/reports/net-zero-by-2050`.

IEA, 2022. *World Energy Outlook 2022.* IEA, Paris. URL `https://www.iea.org/reports/net-zero-by-2050`.

IPCC, 2022. Summary for Policymakers. In: *Climate Change 2022: Mitigation of Climate Change. Contribution of Working Group III to the Sixth Assessment Report of the Intergovernmental Panel on Climate Change*, Cambridge University Press, Cambridge, UK and New York, NY, USA. doi:10.1017/9781009157926.001. URL `https://www.ipcc.ch/report/ar6/wg3/`.

Ivashnyov, O. E., Ivashneva, M. N., Smirnov, N. N., 2000. Slow waves of boiling under hot water depressurization. *J. Fluid Mech.* 413, 149–180. doi:10.1017/S0022112000008417.

Jie, H. E., Xu, B. P., Wen, J. X., Cooper, R., Barnett, J., Sep. 2012. Predicting the decompression characteristics of carbon dioxide using computational fluid dynamics. In: *9th International Pipeline Conference IPC2012.* ASME, IPTI, Calgary, Canada, pp. 585–595. doi:10.1115/IPC2012-90649.

Kunz, O., Wagner, W., October 2012. The GERG-2008 wide-range equation of state for natural gases and other mixtures: An expansion of GERG-2004. *J. Chem. Eng. Data* 57 (11), 3032–3091. doi:10.1021/je300655b.

Le Martelot, S., Saurel, R., Nkonga, B., 2014. Towards the direct numerical simulation of nucleate boiling flows. *Int. J. Multiphase Flow* 66, 62–78. doi:10.1016/j.ijmultiphaseflow.2014.06.010.

LeVeque, R. J., 2002. *Finite Volume Methods for Hyperbolic Problems.* Cambridge University Press, Cambridge, UK. ISBN 0-521-00924-3.

Liao, Y., Lucas, D., Aug. 2017. Computational modelling of flash boiling flows: A literature survey. *Int. J. Heat Mass Tran.* 111, 246–265. doi:10.1016/j.ijheatmasstransfer.2017.03.121.

Linga, G., Flåtten, T., Sep. 2019. A hierarchy of non-equilibrium two-phase flow models. *ESAIM: ProcS* 66, 109–143. doi:10.1051/proc/201966006.

Liu, B., Liu, X., Lu, C., Godbole, A., Michal, G., Tieu, A. K., Feb. 2017. Multi-phase decompression modeling of CO_2 pipelines. *Greenh. Gas. Sci. Tech.* 7 (4), 665–679. doi:10.1002/ghg.1666.

Liu, B., Liu, X., Lu, C., Godbole, A., Michal, G., Tieu, A. K., Oct. 2018. A CFD decompression model for CO_2 mixture and the influence of non-equilibrium phase transition. *Appl. Energ.* 227, 516–524. doi:10.1016/j.apenergy.2017.09.016.

Log, A. M., Jun. 2020. *Development and investigation of HLLC-type finite-volume methods for one and two-phase flow in pipes with varying cross-sectional area.* Master's thesis, Norwegian University of Science and Technology. URL `https://alexandramlog.wordpress.com/2020/12/14/masters-thesis/`.

Log, A. M., Hammer, M., Deng, H., Austegard, A., Hafner, A., Munkejord, S. T., 2023. Depressurization of CO_2 in pipes: Effect of initial state on non-equilibrium two-phase flow – dataset. Zenodo. doi:10.5281/zenodo.7669536.

Log, A. M., Munkejord, S. T., Hammer, M., Hafner, A., Deng, H., Austegard, A., Jun. 2022. Investigation of non-equilibrium effects during the depressurization of carbon dioxide. In: *15th IIR-Gustav Lorentzen Conference on Natural Refrigerants (GL2022). Proceedings. Trondheim, Norway, June 13-15th 2022.* International Institute of Refrigeration (IIR). doi:10.18462/iir.gl2022.0197.

Lund, H., Dec. 2012. A hierarchy of relaxation models for two-phase flow. *SIAM J. Appl. Math.* 72 (6), 1713-1741. doi:10.1137/12086368X.

Lund, H., Aursand, P., 2012. Two-phase flow of CO_2 with phase transfer. In: Røkke, N. A., Hägg, M.-B., Mazzetti, M. J. (Eds.), *6th Trondheim Conference on CO_2 Capture, Transport and Storage (TCCS-6).* BIGCCS / SINTEF / NTNU, Energy Procedia vol. 23, Trondheim, Norway, pp. 246–255.

doi:10.1016/j.egypro.2012.06.034.

Martynov, S., Zheng, W., Mahgerefteh, H., Brown, S., Hebrard, J., Jamois, D., Proust, C., 2018. Computational and experimental study of solid-phase formation during the decompression of high-pressure CO_2 pipelines. *Ind. Eng. Chem. Res.* 57 (20), 7054–7063. doi:10.1021/acs.iecr.8b00181.

Michal, G., Østby, E., Davis, B. J., Røneid, S., Lu, C., Sep. 2020. An empirical fracture control model for dense-phase CO2 carrying pipelines. In: *13th International Pipeline Conference, IPC 2020*. ASME. doi:10.1115/IPC2020-9421.

Munkejord, S. T., Austegard, A., Deng, H., Hammer, M., Stang, H. G. J., Løvseth, S. W., Nov. 2020. Depressurization of CO_2 in a pipe: High-resolution pressure and temperature data and comparison with model predictions. *Energy* 211, 118560. doi:10.1016/j.energy.2020.118560.

Munkejord, S. T., Deng, H., Austegard, A., Hammer, M., Skarsvåg, H. L., Aasen, A., Jul. 2021. Depressurization of CO_2-N_2 and CO_2-He in a pipe: Experiments and modelling of pressure and temperature dynamics. *Int. J. Greenh. Gas Con.* 109, 103361. doi:10.1016/j.ijggc.2021.103361.

Munkejord, S. T., Hammer, M., Jun. 2015. Depressurization of CO_2-rich mixtures in pipes: Two-phase flow modelling and comparison with experiments. *Int. J. Greenh. Gas Con.* 37, 398–411. doi:10.1016/j.ijggc.2015.03.029.

Munkejord, S. T., Hammer, M., Løvseth, S. W., May 2016. CO_2 transport: Data and models – A review. *Appl. Energ.* 169, 499–523. doi:10.1016/j.apenergy.2016.01.100.

Nakagawa, M., Berana, M. S., Kishine, A., 2009. Supersonic two-phase flow of CO_2 through converging-diverging nozzles for the ejector refrigeration cycle. *Int. J. Refrig.* 32 (6), 1195–1202. doi:10.1016/j.ijrefrig.2009.01.015.

Pelanti, M., 2022. Arbitrary-rate relaxation techniques for the numerical modeling of compressible two-phase flows with heat and mass transfer. *Int. J. Multiphase Flow* 153, 104097. doi:10.1016/j.ijmultiphaseflow.2022.104097.

Pinhasi, G. A., Ullmann, A., Dayan, A., Aug. 2005. Modeling of flashing two-phase flow. *Reviews in Chemical Engineering* 21 (3-4), 133–264. doi:10.1515/REVCE.2005.21.3-4.133.

Quinn, D., Stannard, D., Edwards, J., Botros, K. K., Johansen, C., 2022. Experimental visualization and characteristics of bubble nucleation during rapid decompression of supercritical and subcooled carbon dioxide. *Int. J. Pres. Ves. Pip.* 195, 104569. doi:10.1016/j.ijpvp.2021.104569.

Roussanaly, S., Bureau-Cauchois, G., Husebye, J., Jan. 2013. Costs benchmark of CO_2 transport technologies for a group of various size industries. *Int. J. Greenh. Gas Con.* 12, 341–350. doi:10.1016/j.ijggc.2012.05.008.

Saurel, R., Boivin, P., Le Métayer, O., Mar. 2016. A general formulation for cavitating, boiling and evaporating flows. *Comput. Fluids* 128, 53–64. doi:10.1016/j.compfluid.2016.01.004.

Skarsvåg, H. L., Hammer, M., Munkejord, S. T., Log, A. M., Dumoulin, S., Gruben, G., Mar. 2023. Towards an engineering tool for the prediction of running ductile fractures in CO_2 pipelines. *Process Saf. Environ.* 171, 667–679. doi:10.1016/j.psep.2023.01.054.

Span, R., Wagner, W., Nov.–Dec. 1996. A new equation of state for carbon dioxide covering the fluid region from the triple-point temperature to 1100 K at pressures up to 800 MPa. *J. Phys. Chem. Ref. Data* 25 (6), 1509–1596. doi:10.1063/1.555991.

Teng, L., Li, Y., Zhao, Q., Wang, W., Hu, Q., Ye, X., Zhang, D., Nov. 2016. Decompression characteristics of CO_2 pipelines following rupture. *J. Nat. Gas Sci. Eng.* 36 (A), 213–223. doi:10.1016/j.jngse.2016.10.026.

Toro, E. F., 2009. *Riemann solvers and numerical methods for fluid dynamics: A practical introduction*. Springer-Verlag, Berlin, third ed. ISBN 978-3-540-25202-3.

Toro, E. F., Spruce, M., Speares, W., 1994. Restoration of the contact surface in the HLL-Riemann solver. *Shock Waves* 4 (1), 25–34.

Wilhelmsen, Ø., Aasen, A., 2022. Choked liquid flow in nozzles: Crossover from heterogeneous to homogeneous cavitation and insensitivity to depressurization rate. *Chem. Eng. Sci.* 248, 117176. doi:10.1016/j.ces.2021.117176.

Wilhelmsen, Ø., Aasen, A., Skaugen, G., Aursand, P., Austegard, A., Aursand, E., Gjennestad, M. A., Lund, H., Linga, G., Hammer, M., 2017. Thermodynamic modeling with equations of state: Present challenges with established methods. *Ind. Eng. Chem. Res.* 56 (13), 3503–3515. doi:10.1021/acs.iecr.7b00317.

Winters, W. S., Jr., Merte, J. H., 1979. Experiments and Nonequilibrium Analysis of Pipe Blowdown. *Nucl. Sci. Eng.* 69 (3), 411–429. doi:10.13182/NSE79-A19959.

Xiao, C., Lu, Z., Yan, L., Yao, S., 2020. Transient behaviour of liquid CO_2 decompression: CFD modelling and effects of initial state parameters. *Int. J. Greenh. Gas Con.* 101, 103154. doi:10.1016/j.ijggc.2020.103154.

Appendix A. The homogeneous superheat limit

We here present details on how the homogeneous superheat limit can be estimated using classical nucleation theory. The superheat limit can be considered the experimentally obtainable superheat achieved before sudden phase change is observed. This limit is assumed to be connected to the rate of bubble formation, or "nucleation" rate.

Generally, nucleation is divided into two categories: homogeneous and heterogeneous nucleation. Homogeneous nucleation occurs in the bulk of the liquid and is caused by random density fluctuations in the liquid creating bubbles large enough to grow and not collapse back into the liquid phase. In order to create a stable bubble, an activation energy must be reached. Heterogeneous nucleation occurs on a surface like a wall or an impurity, lowering the activation energy of nucleation.

The experimentally achievable superheat limit can be estimated using classical nucleation theory (CNT), which models homogeneous nucleation. CNT provides a formal estimate on the nucleation rate of critically-sized embryos of a new phase in the mother phase. Here, critically-sized is defined as the size where the embryo is just large enough not to collapse back to the mother phase. The derivation of this rate is presented by Debenedetti (1997), and we here simply state the resulting equations.

The nucleation rate (critically-sized embryos formed per volume and time) is defined as an Arrhenius-type rate law,

$$J = K \exp\left(-\frac{\Delta G^*}{k_B T_\ell}\right), \tag{A.1}$$

where ΔG is the free-energy barrier of embryo formation, k_B is the Boltzmann constant and K is a kinetic prefactor. The superscript $*$ denotes properties of a critically-sized embryo. For the formation of bubbles in a superheated liquid, the free-energy barrier is estimated to be

$$\Delta G^* = \frac{4\pi \sigma r^{*2}}{3}, \tag{A.2}$$

where σ denotes the surface tension and r the radius of the bubble. It is assumed that the surface tension of the bubble, σ, is equal to the macroscopic surface tension of a planar interface between the liquid and vapor at equilibrium.

The critical radius of the bubble is approximated as

$$r^* = \frac{2\sigma}{p_{\text{sat}}(T_\ell) - p_\ell}, \tag{A.3}$$

where $p_{\text{sat}}(T_\ell)$ is the saturation pressure at the temperature of the liquid. The kinetic prefactor can be approximated as

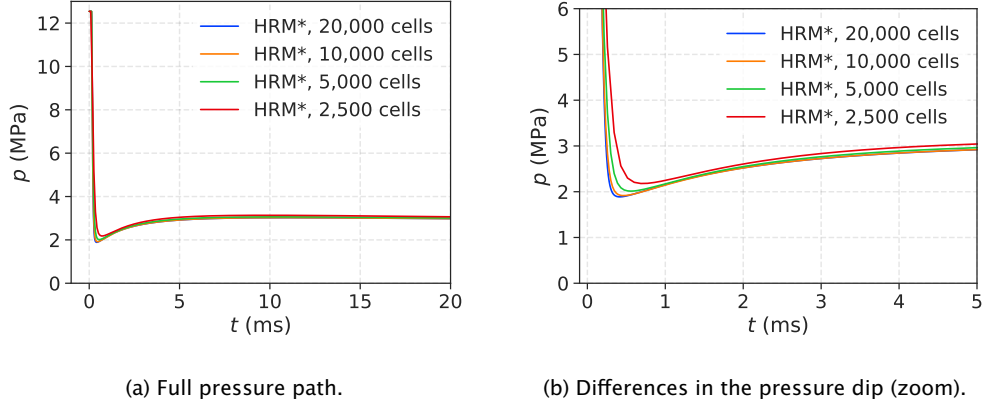$$K = \tilde{\rho}_\ell \sqrt{\frac{2\sigma}{\pi m}}, \tag{A.4}$$

(a) Full pressure path. (b) Differences in the pressure dip (zoom).

Figure B.21: Simulated pressure trace (HRM*) at $x = 0.08\,\text{m}$ for 2,500, 5,000, 10,000 and 20,000 grid cells for the initial condition of Test 4.

where m is the mass of one molecule and $\tilde{\rho}_\ell = \rho_\ell/m$ is the number density of molecules in the liquid. With these relations, the superheat limit temperature can be estimated by solving

$$J(T_\ell) = J_{\text{crit}} \tag{A.5}$$

for T_ℓ. Here, J_{crit} is the critical nucleation rate, at which sudden phase change is observed. In this work, we follow Aursand *et al.* (2016b), employing $J_{\text{crit}} = 1 \times 10^{12}\,\text{m}^{-3}\,\text{s}^{-1}$. Due to the exponential functional form in (A.1), the superheat limit is not very sensitive to the critical rate.

Appendix B. Grid-refinement study

In order to determine an appropriate number of grid cells applied in the simulations, a grid refinement study is conducted. With the assumption that the results will hold for all the initial conditions studied in this work, the grid-refinement is conducted for the conditions of Test 4. We test grids with 2,500, 5,000, 10,000 and 20,000 grid cells. The simulations are conducted up to $t_{\text{end}} = 20\,\text{ms}$ and the relaxation time for the mass-transfer source term is set to $\theta = 2\,\text{ms}$. The results are presented in Figures B.21 and B.22.

Figure B.21 shows the pressure traces simulated using the HRM* for the different grids at $x = 0.08\,\text{m}$. The result of the different grids nearly overlap, but the lowest point of the pressure undershoot becomes lower for finer grids and occurs earlier in time. This effect is smaller further inside the pipe. In Figure B.22, we show that the pressure waves become sharper for finer grids, as expected. The sharper pressure drop is likely causing the change in the pressure undershoot as a faster pressure drop allows for further penetration into the metastable region before delayed gas nucleation begins. The simulation with 2,500 grid cells predicts the lowest point in the pressure dip to be approximately $0.3\,\text{MPa}$ higher than that with 20,000 grid cells. For 5,000 grid cells, this difference is $0.13\,\text{MPa}$ and the difference is around $0.03\,\text{MPa}$
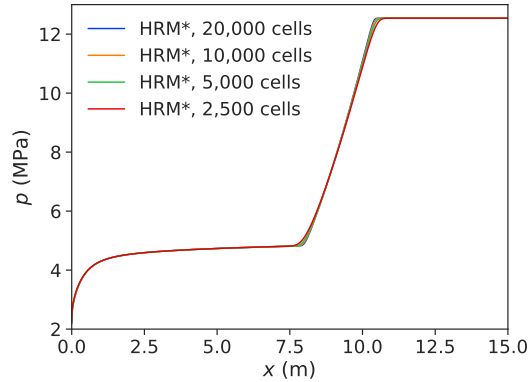
41

Figure B.22: Simulated pressure (HRM*) along the pipe at $t = 20$ ms for 2,500, 5,000, 10,000 and 20,000 grid cells for the initial condition of Test 4.
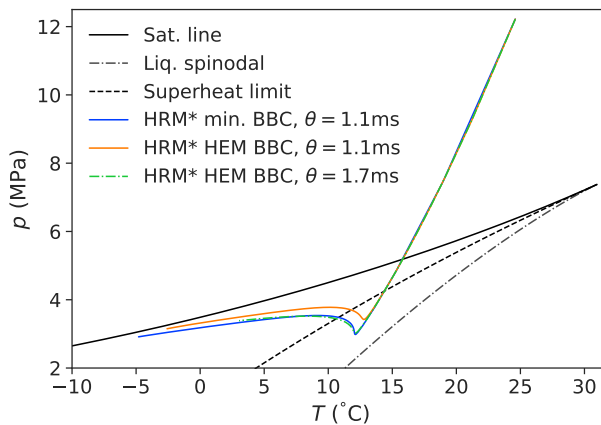

Figure C.23: Effect of different settings for the outflow BC for Test 8. p-T paths simulated by the HRM* $x = 3$ mm from the open end of the pipe.

for 10,000 grid cells. Based on these results, we choose to apply 10,000 grid cells for the simulations in the present paper.

Appendix C. p-T path of the HRM* with the HEM outflow boundary condition

The pressures predicted by HRM* matches experimentally measured pressure undershoots well, but the calculated superheats are quite high. In this section, we investigate whether the HRM* predicts a smaller superheat if we apply the HEM BBC instead of the minimum BBC as the outflow BC. The HEM BBC assumes that the flow occurs in equilibrium, such that the fluid state is locked to the saturation line for two-phase flow. Generally, this will lead to a higher choking pressure at the boundary than what is predicted by the minimum BBC.
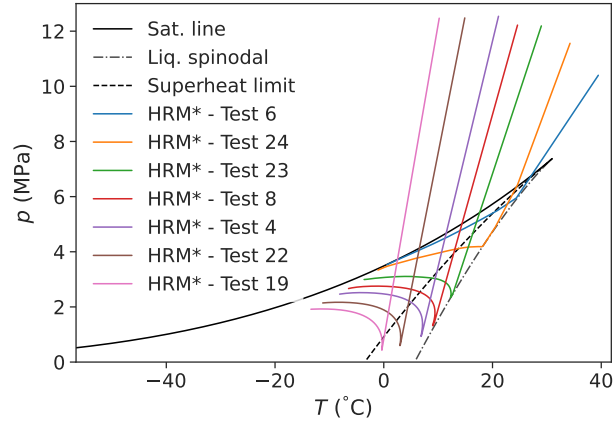
42

Figure D.24: Effect of initial condition on the depressurization process: The p-T paths simulated by the HRM* in the first grid cell of the computational domain, at $x = 3$ mm from the open end of the pipe.

In Figure C.23, we compare the p-T-paths predicted by the HRM* for Test 8 applying the minimum BBC with $\theta = 1.1$ ms, and the HEM BBC with $\theta = 1.1$ ms and $\theta = 1.7$ ms at $x = 3$ mm from the open end. As the HEM BBC enforces a higher choking pressure, the pressure undershoot becomes smaller with this BBC than for the minimum BBC with the same relaxation time in the mass-transfer rate. If the relaxation time in the HRM* is increased for the HEM BBC to $\theta = 1.7$ ms, the same pressure undershoot can be reached as for the minimum BBC with $\theta = 1.1$ ms.

The relaxation time is chosen to fit the pressure undershoot measured in the experiments i.e. $\theta = 1.7$ ms for the HEM BBC. Though the pressure recovery becomes slightly different for the HEM BBC, the degree of superheat reached is the same for the HRM* with both BCs. This means that the large superheat predicted by the HRM* is not caused by the minimum BBC, but by the mass-transfer model. To reduce computational costs, these simulations were run with 1,000 grid cells, but the results apply for finer grids as well.

Appendix D. p-T path in the first grid cell and the outflow ghost cell

In Figure D.24, we show the simulated p-T paths for all the tests in the first grid cell of the computational domain, which has its cell center at 3 mm from the open end. For this grid cell, the simulated depressurization path of Tests 6, 8, 23 and 24 reaches the liquid spinodal. For these tests, the relaxation times are at their maximum value. If a longer relaxation time is chosen, the simulations will crash as the liquid phase will pass into the unstable domain.

In Figure D.25, we show the simulated p-T-paths for all the experiments in the outflow ghost cell. It is clear that the method where the choking pressure for the BC is searched for by "walking" along the spinodal (see Section 4.2) is needed for the four warmest experiments, Tests 6, 8, 23 and 24.
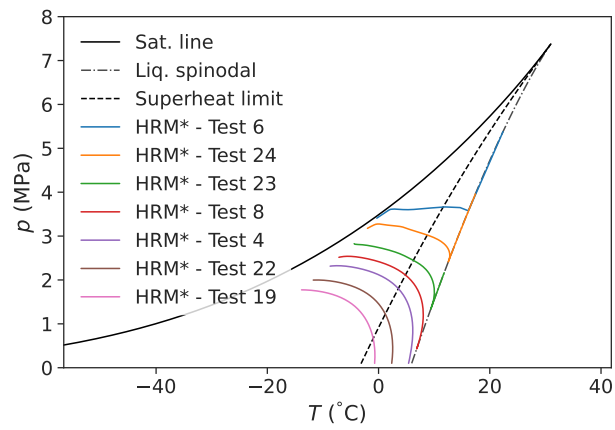
Figure D.25: The p-T paths simulated by the HRM* in the outflow ghost cell, at $x = -3\,\text{mm}$ from the open end of the pipe.